REPRODUCED AT GOVERNMENT EXPENSE

AFOSR-TR- 84-1102

L2

AD-A148 528

RESPONSE OF SATURATED POROUS NONLINEAR MATERIALS TO DYNAMIC LOADINGS

Approved for Public Release;
Distribution unlimited.

DTIC FILE COPY

DTIC
ELECTE
DEC 13 1984
S D
D

APPLIED RESEARCH ASSOCIATES, INC.
Engineering and Applied Science

84 12 03 173

Accession For
NTIS GRA&I
DTIC TAB
Unannounced
Justification
By
Distribution/
Availability Codes
Dist | Avail and/or Special
A-1

AIR FORCE OFFICE OF SCIENTIFIC RESEARCH (AFSC)
NOTICE OF TRANSMITTAL DTIC
This technical report has been reviewed and is approved for public release IAW AFR 190-12.
Distribution is unlimited.
MATTHEW J. KERPER
Chief, Technical Information Division

RESPONSE OF SATURATED POROUS NONLINEAR MATERIALS TO DYNAMIC LOADINGS

31 May 1984

Prepared for
Air Force Office of Scientific Research
Washington, D.C.

Prepared under
Contract No. F49620-81-C-0014

DTIC
ELECTE
DEC 13 1984
S D
D

Kwang Jin Kim
Scott E. Blouin

Applied Research Associates, Inc.
New England Division
South Royalton, Vermont 05068

UNCLASSIFIED
SECURITY CLASSIFICATION OF THIS PAGE

REPORT DOCUMENTATION PAGE

1a. REPORT SECURITY CLASSIFICATION: UNCLASSIFIED	1b. RESTRICTIVE MARKINGS
2a. SECURITY CLASSIFICATION AUTHORITY	3. DISTRIBUTION/AVAILABILITY OF REPORT: Approved for Public Release; Distribution Unlimited.
2b. DECLASSIFICATION/DOWNGRADING SCHEDULE	
4. PERFORMING ORGANIZATION REPORT NUMBER(S): [redacted]	5. MONITORING ORGANIZATION REPORT NUMBER(S): AFOSR-TR- 84-1102
6a. NAME OF PERFORMING ORGANIZATION: APPLIED RESEARCH ASSOCIATES, INC. (6b. OFFICE SYMBOL (If applicable))	7a. NAME OF MONITORING ORGANIZATION: AFOSR/NA
6c. ADDRESS (City, State and ZIP Code): NEW ENGLAND DIVISION, SOUTH ROYALTON, VT 05068	7b. ADDRESS (City, State and ZIP Code): Bolling AFB, DC 20332-6448
8a. NAME OF FUNDING/SPONSORING ORGANIZATION: AIR FORCE OFFICE OF SCIENTIFIC RESEARCH (8b. OFFICE SYMBOL (If applicable): AFOSR/NA)	9. PROCUREMENT INSTRUMENT IDENTIFICATION NUMBER: F49620-81-C-0014
8c. ADDRESS (City, State and ZIP Code): BOLLING AFB, DC 20332	10. SOURCE OF FUNDING NOS. — PROGRAM ELEMENT NO.: 61102F; PROJECT NO.: 2307; TASK NO.: C1; WORK UNIT NO.:
11. TITLE (Include Security Classification): RESPONSE OF SATURATED POROUS NONLINEAR MATERIALS TO DYNAMIC LOADINGS (UNCLASSIFIED)	
12. PERSONAL AUTHOR(S): KWANG J. KIM, SCOTT E. BLOUIN	
13a. TYPE OF REPORT: FINAL	13b. TIME COVERED: FROM _____ TO _____
14. DATE OF REPORT (Yr., Mo., Day): 31 MAY 1984	15. PAGE COUNT: 100
16. SUPPLEMENTARY NOTATION	

17. COSATI CODES		
FIELD	GROUP	SUB. GR.

18. SUBJECT TERMS (Continue on reverse if necessary and identify by block number): Finite element modeling, soil mechanics, liquefaction, blast-induced liquefaction, soil dynamics

19. ABSTRACT (Continue on reverse if necessary and identify by block number)

Past theoretical treatments of two phase media are reviewed and incorporated into the two phase dynamic finite element code TPDAP. A study of the response of two phase porous elastic media to dynamic uniaxial loadings is conducted and the influence of loading shape, material properties, and numerical techniques and parameters are evaluated. A series of calculations simulating uniaxial loadings of saturated soils having hysteretic skeletons is conducted. Zones of liquefaction occuring in these calculations are identified and the mechanics of liquefaction and influence of parametric variations on liquefaction are investigated and described.

20. DISTRIBUTION/AVAILABILITY OF ABSTRACT: UNCLASSIFIED/UNLIMITED ☐ SAME AS RPT. ☐ DTIC USERS ☐	21. ABSTRACT SECURITY CLASSIFICATION: UNCLASSIFIED
22a. NAME OF RESPONSIBLE INDIVIDUAL: Lt Col Lawrence D Hokanson	22b. TELEPHONE NUMBER (Include Area Code): 202-767-4935 — 22c. OFFICE SYMBOL: AFOSR/NA

DD FORM 1473, 83 APR — EDITION OF 1 JAN 73 IS OBSOLETE.

UNCLASSIFIED
SECURITY CLASSIFICATION OF THIS PAGE

TABLE OF CONTENTS

SECTION 1

INTRODUCTION

Blast induced liquefaction has been identified as an important mechanism in the development of craters and ground motions from large explosions in or on saturated soil deposits. Liquefaction may have dominated crater formation processes in the saturated geologies of the Pacific Proving Grounds where all the high yield U.S. nuclear cratering data were obtained. Based on analysis of these and other high explosive test data from sites having shallow water tables within the continental United States and Canada, Blouin and Shinn (1983) hypothesized liquefaction and cratering mechanisms controlled by the liquefaction which explain the unusually flat broad shapes of these craters. Based on their hypothesis, it was concluded that current cratering prediction procedures founded on the Pacific data are not valid for dry continental sites. The data analysis indicates that water table will influence the crater formation processes whenever the scaled depth of the water table is less than about 7 $ft/ton^{1/3}$, where the yield is expressed as an equivalent high explosive half buried yield. It was also concluded, however, that many so called dry sites may actually behave like wet sites, because scaled water table depths for the high yield nuclear threats of interest are quite shallow.

This previous work also included formulation of liquefaction mechanisms due to explosive loadings. Application of those mechanisms was limited by the simplifying assumptions used to derive the analytic equations.

More precise methods to analyze and predict the occurrence of blast induced liquefaction must rely on two phase dynamic numerical computer codes. Such codes can incorporate complicated models of real world material properties with accurate characterization of actual explosive loading functions to determine the dynamic response of saturated geologic media. The complexity of the real world material properties, loading functions and problem geometries puts realistic depiction of the dynamic response beyond the reach of conventional analytic techniques.

In general terms, two phase dynamic codes compute the response of saturated porous media to static or dynamic loadings. The media are modeled by combining the response characteristics of the soil skeleton with the response characteristics of the pore water using two equations. The first of these describes the motion of the bulk soil-water mixture as a function of the applied load and the second describes the motion of the pore fluid relative to the soil skeleton under the applied load. The dynamic response of the saturated material is expressed in terms of the intergranular or effective stress in the soil skeleton, the absolute motion of the soil skeleton, the pressure in the pore water, and the motion of the pore water relative to the soil skeleton. Presentation of the calculational results in terms of the response of each separate phase makes the two phase codes extremely powerful tools for the study of blast induced liquefaction.

The objectives of this study are to review and condense past theoretical treatments of two phase media, to incorporate these results in the Two Phase Dynamic Analysis Program (TPDAP), to use TPDAP to study the response of saturated porous media to dynamic loadings, and to identify and analyze liquefaction occurring in these calculations. Procedures used in, and results of this study are described in the following three sections. The objectives and content of each section are summarized below.

SECTION 2: Fundamental theoretical treatments of two phase porous media by Biot and others are reviewed. Biot's fluid equation describing the interactions between the pore fluid and soil skeleton is generalized and incorporated into the finite element code TPDAP. Also, a general description of TPDAP is presented.

SECTION 3: A series of parametric calculations of the response of two phase porous elastic media to dynamic uniaxial loadings is conducted. The influence of various loadings, material properties and numerical techniques are described and analyzed.

SECTION 4: A series of parametric calculations on saturated materials having hysteretic soil skeletons is conducted. These include a bilinear material skeleton and an actual sand skeleton. Zones of liquefaction occurring in these calculations are identified and the mechanics of liquefaction and influence of parametric variations on liquefaction are described.

SECTION 2

THEORETICAL DEVELOPMENT AND IMPLEMENTATION

BACKGROUND

The fundamental analytic work describing the behavior of saturated porous media was performed by Biot. Biot's results were reported in a series of papers extending over many years (e.g. 1956, 1962a and 1962b). Other investigators have applied Biot's analytic results using techniques which approximate his equations with varying degrees of accuracy and sophistication (e.g. Ghaboussi and Wilson 1972, Mengi and McNiven, 1977). In this section, we summarize the development of the two phase equations of motion based on Biot's work and their implementation in the two phase finite element code TPDAP.

ANALYTIC DEVELOPMENT

The behavior of saturated porous material can be described in terms of two equations of motion; the first is the equation of motion of the bulk soil-water mixture and the second is the equation of motion of the pore fluid within the soil skeleton.

Governing Equation for Bulk Mixture

The differential equation of motion governing the bulk mixture is given by

$$\sigma_{ij,j} = (1 - n)\rho_s \ddot{u}_i + n \rho_f \ddot{U}_i \qquad (2\text{-}1)$$

$\sigma_{ij,j}$ is the total stress gradient applied to an infinitesimal element of saturated material at some given time. $\sigma_{ij,j}$ is expressed in tensor notation and represents the stress gradient in each of 3 mutually perpendicular coordinates (e.g. see Mendelson, 1968). For instance, in the x direction,

$$\sigma_{xj,j} = \frac{\partial \sigma_{xx}}{\partial_x} + \frac{\partial \sigma_{xy}}{\partial_y} + \frac{\partial \sigma_{xz}}{\partial_z} = (1 - n)\ \rho_s \ddot{u}_x + n\ \rho_f\ \ddot{U}_x \qquad (2\text{-}2)$$

The term $(1 - n)\rho_s$ is the mass of the soil skeleton per unit volume of saturated material, where n is the porosity and ρ_s is the mass density of the solid grains. u_i is the displacement of the skeleton in the i direction and $\ddot{u}_i$ is the acceleration of the skeleton in the i direction. The term $n\rho_f$ is the mass of pore fluid per unit volume of saturated material where ρ_f is the mass density of the pore fluid. U_i is the absolute displacement of the pore fluid in the i direction and $\ddot{U}_i$ the absolute acceleration of the pore fluid in the i direction.

The bulk mass density of the saturated material, ρ, is given by

$$\rho = (1 - n)\rho_s + n\rho_f \qquad (2\text{-}3)$$

Substitution of the value for $(1 - n)\rho_s$ from Equation 2-3 into Equation 2-1 gives

$$\sigma_{ij,j} = (\rho - n\rho_f)\ddot{u}_i + n\rho_f\ddot{U}_i \qquad (2\text{-}4)$$

A term w_i is introduced which is the apparent fluid displacement in the i direction relative to the soil skeleton and is given by

$$w_i = n(U_i - u_i) \tag{2-5}$$

In seepage problems, w_i is referred to as the discharge displacement. It describes the discharge of fluid through a soil mass of unit area. The discharge velocity, or apparent relative velocity, $\dot{w}_i$, between the soil particles and pore water is the velocity of water in a discharge duct of unit area needed to maintain the actual relative velocity in the porous soil of the same unit area. The actual relative velocity between the skeleton and the pore water is given by $\dot{w}_i/n$. Finally, $\ddot{w}_i$ is the apparent relative acceleration between the soil skeleton and pore water given by

$$\ddot{w}_i = n(\ddot{U}_i - \ddot{u}_i) \tag{2-6}$$

Equation 2-4 can be expressed in terms of the apparent relative fluid acceleration as simply

$$\boxed{\sigma_{ij,j} = \rho\ddot{u}_i + \rho_f\ddot{w}_i} \tag{2-7}$$

Governing Equation for Pore Fluid

Biot's Equations

The equation of motion governing the pore fluid is derived from Biot's work (see previous references). Biot expressed the pore pressure gradient, $\pi_{,i}$, as

$$\pi_{,i} = \rho_f \ddot{U}_i + D_i \tag{2-8}$$

In this equation, the pore pressure gradient is expressed in tensor notation. For example, the gradient in the x direction is given by

$$\pi_{,x} = \rho_f \ddot{U}_x + D_x \qquad (2\text{-}9)$$

The term $\rho_f \ddot{U}_i$ is the inertial force per unit volume of pore fluid. D_i represents the viscous friction force between the pore fluid and the soil skeleton per unit volume of pore fluid. Solving Equation 2-6 for $\ddot{U}_i$ and substitution into Equation 2-8 gives

$$\pi_{,i} = \frac{\rho_f}{n} \ddot{w}_i + \rho_f \ddot{u}_i + D_i \qquad (2\text{-}10)$$

Biot showed that the viscous friction term, D_i, is a function of the excitation frequency, ω, the pore geometry, the dynamic viscosity, μ, and the apparent relative velocity between the pore fluid and the skeleton, $\dot{w}_i$. In an actual soil the flow of pore water would follow very complicated paths which are difficult to describe. These flow paths would involve numerous variations in direction and in cross sectional area. Biot employed models of the flow paths which are gross simplifications of the actual paths. He assumed two simple flow geometries; flow through a series of parallel circular ducts and flow through a series of parallel flat ducts. Biot derived equations describing the pore fluid flow in these two simplified pore geometries.

Flow conditions in the flat duct are pictured schematically in Figure 2.1. The duct is assumed to have infinite width and a height 2a. Flow is considered over a unit width of duct having a cross sectional area of 2a. Biot (1956) expresses the ratio of viscous shear force 2τ, (where τ is the viscous shear stress) to the average fluid velocity relative to the duct walls, $\dot{w}_{ai}$, as

$$\frac{2\tau}{\dot{w}_{ai}} = \frac{6\mu}{a} F(\kappa) \qquad (2\text{-}11)$$

The average relative velocity is given by

$$\dot{W}_{ai} = \dot{U}_{ai} - \dot{u}_i \qquad (2\text{-}12)$$

where $\dot{U}_{ai}$ is the average absolute fluid velocity in the duct and $\dot{u}_i$ the velocity of the duct walls. μ is the dynamic viscosity (dyne-sec/cm^2) and $F(\kappa)$ is a complex function of frequency which describes the increase in viscous shear with frequency. Biot (1956) gives an equation for F of

$$F(z) = \frac{1}{3} \frac{z \tanh(z)}{1 - \frac{1}{z} \tanh(z)} \qquad (2\text{-}13)$$

where

$$z = i^{1/2} \kappa \qquad (2\text{-}14)$$

and

$$\kappa = a \left(\frac{\rho_f \omega}{\mu} \right)^{1/2} \qquad (2\text{-}15)$$

Thus, κ is a function of the duct dimension, a, the dynamic viscosity, μ, the fluid density, ρ_f, and the excitation frequency ω. The friction force per unit volume of pore fluid, D_i from Equation 2-6, is given by

$$D_i = \frac{2\tau}{2a} \qquad (2\text{-}16)$$

Substitution of Equation 2-11 into 2-16 gives

$$\boxed{D_i = \frac{3\mu}{a^2} F(\kappa) \dot{W}_i} \qquad (2\text{-}17)$$

for the flat duct.

Flow conditions in the circular duct are pictured schematically in Figure 2.2. In this case, a represents the radius of the duct having a cross sectional area of πa^2. Biot (1956) gives the ratio of viscous shear force, $2\pi a\tau$, to the average relative fluid velocity, $\dot{W}_{ai}$, as

$$\frac{2\pi a\tau}{\dot{W}_{ai}} = 8\pi\mu F(\kappa) \qquad (2\text{-}18)$$

For the circular duct,

$$F(\kappa) = \frac{1}{4} \frac{\kappa T(\kappa)}{1 - \frac{2}{i\kappa} T(\kappa)} \qquad (2\text{-}19)$$

where κ is given in Equation 2-15, with, a, now equal to the radius of the circular duct and the function $T(\kappa)$ given by

$$T(\kappa) = \frac{\frac{\partial}{\partial\kappa}\left(J_o\left(i^{3/2}\kappa\right)\right)}{J_o\left(i^{3/2}\kappa\right)} \qquad (2\text{-}20)$$

J_o represents Bessel's function for n = 0 and is given by

$$J_o(x) = 1 - \frac{x^2}{4} + \frac{x^4}{64} - \frac{x^6}{2304} + \ldots. \qquad (2\text{-}21)$$

where $$x = i^{3/2} \kappa \qquad (2\text{-}22)$$

The friction force per unit volume of pore fluid in the circular duct D_i from Equation 2-8, is given by

$$D_i = \frac{2\pi a \tau}{\pi a^2} \qquad (2\text{-}23)$$

Substitution of Equation 2-18 into 2-23 gives

$$\boxed{D_i = \frac{8\mu}{a^2} F(\kappa) \dot{w}_i} \qquad (2\text{-}24)$$

for the circular duct.

Biot's Approximations for Viscous Shear

Biot (1962b) derived an approximation for the viscous friction correction factor, $F(\kappa)$, for the case of a flat duct, over a limited range of frequencies. An alternative derivation to that used by Biot is presented here. For the flat duct, the viscous correction factor is given by Equation 2-13. If tanh(z) is expressed as

$$\tanh(z) = z - \frac{1}{3} z^3 + \frac{2}{15} z^5 - \ldots. \qquad (2\text{-}25)$$

then

$$z \tanh(z) = z^2 - \frac{1}{3} z^4 + \frac{2}{15} z^6 - .... \quad (2\text{-}26)$$

and

$$1 - \frac{1}{z} \tanh(z) = \frac{1}{3} z^2 - \frac{2}{15} z^4 + ... \quad (2\text{-}27)$$

Substitution of Equations 2-14, 2-26 and 2-27 into Equation 2-13 gives an approximation for the flat duct of

$$\boxed{F(\kappa) = 1 + \frac{1}{15} (i\kappa^2) + ...} \quad (2\text{-}28)$$

when higher order terms above κ^2 are dropped. This agrees with Biot's approximation. Biot indicates that the above approximation is accurate to within 5% for values of frequency of

$$\omega \leq \frac{3\mu}{a^2 \rho_f} \quad (2\text{-}29)$$

and represents a reasonable approximation of $F(\kappa)$ up to a frequency of about

$$\omega < \frac{12\mu}{a^2 \rho_f} \quad (2\text{-}30)$$

For a pore size of $a = .005$ cm and water at 15°C ($\mu/\rho_f = .013$ cm^2/sec) Biot indicates that Equation 2-27 is accurate up to approximately 300 Hz. Mengi and McNiven (1977) determined that Biot's

approximation given in Equation 2-27 is accurate even for the abrupt stress changes at a wavefront.

A similar approach can be used to obtain an approximation of the viscous correction factor for the circular duct given by Equation 2-19. Evaluating $T(\kappa)$ according to Equations 2-20 and 2-21 gives

$$T(\kappa) = \frac{1}{2} i\kappa + \frac{1}{16} \kappa^3 - \frac{1}{96} i\kappa^5 + ... \quad (2\text{-}31)$$

Substitution of Equation 2-31 into 2-19 gives the approximation for $F(\kappa)$ in the case of the circular duct of

$$\boxed{F(\kappa) \simeq 1 + \frac{1}{24} (i\kappa^2) + ...} \quad (2\text{-}32)$$

when higher order terms above κ^2 are dropped.

Biot (1956) indicates that there is an approximate equivalence between the circular duct and the flat duct, when the height of the flat duct equals 3/4 of the diameter of the circular duct. Applying this equivalence to Equations 2-29 and 2-30 indicates that Equation 2-32 for the circular duct is reasonably accurate up to frequencies of nearly twice that of a flat duct if the respective diameters and heights are equal.

The expressions for the viscous friction correction factors from Equations 2-28 and 2-32 for the flat and circular ducts respectively can be substituted into Equations 2-17 and 2-24 to give the friction force per unit volume of pore fluid in each type of duct. For the flat duct this yields

$$D_i = \frac{3\mu}{a^2} \dot{w}_i + \frac{\mu}{5a^2} i\kappa^2 \dot{w}_i \quad (2\text{-}33)$$

and for the circular duct

$$D_i = \frac{8\mu}{a^2}\dot{W}_i + \frac{\mu}{3a^2} i\kappa^2 \dot{W}_i \qquad (2\text{-}34)$$

As discussed previously, the actual relative velocity between the skeleton and the pore fluid, $\dot{W}_i$, is given by

$$\dot{W}_i = \frac{1}{n}\dot{w}_i \qquad (2\text{-}35)$$

Substitution of Equations 2-35 and 2-15 into Equation 2-33 gives the friction force per unit volume of pore fluid for the flat duct as

$$D_i = \frac{3\mu}{na^2}\dot{w}_i + \frac{\rho_f}{5n} i\omega\dot{w}_i \qquad (2\text{-}36)$$

For an input excitation of frequency ω, the excitation velocity can be expressed as

$$\dot{w}_i = \dot{\bar{w}}_i e^{i\omega t} \qquad (2\text{-}37)$$

where $\dot{\bar{w}}_i$ is the amplitude of the excitation velocity. Differentiating Equation 2-37 with respect to time gives the apparent relative acceleration, $\ddot{w}_i$, as

$$\ddot{w}_i = i\omega\dot{\bar{w}}_i e^{i\omega t} = i\omega\dot{w}_i \qquad (2\text{-}38)$$

Thus, Equation 2-36 for the flat duct can be rewritten as

$$D_i = \frac{3\mu}{na^2}\dot{w}_i + \frac{\rho_f}{5n}\ddot{w}_i \qquad (2\text{-}39)$$

For the circular duct substitution of Equations 2-35 and 2-15 into Equation 2-34 gives

$$D_i = \frac{8\mu}{na^2}\dot{w}_i + \frac{\rho_f}{3n}\, i\omega\dot{w}_i \qquad (2\text{-}40)$$

Finally, substitution of Equation 2-38 into 2-40 gives

$$D_i = \frac{8\mu}{na^2}\dot{w}_i + \frac{\rho_f}{3n}\ddot{w}_i \qquad (2\text{-}41)$$

Even though Equations 2-39 and 2-41 were derived assuming a single harmonic forcing function, it can be demonstrated that they should apply for any arbitrary excitation. Since any arbitrary excitation function can be decomposed into an infinite series of harmonic functions, each of these excitations can be treated by the above equations and the total friction force obtained by superimposing the contribution from each harmonic excitation of the decomposed total input.

Application of Darcy's Law

Biot's equations, based on thermodynamic theory, can be related to Darcy's flow Law. Darcy's Law assumes that the flow velocity is proportional to the hydraulic gradient. For an arbitrary gradient, the equivalent permeability coefficients can be derived analytically for both the flat and circular ducts. These permeability coefficients can then be compared to Biot's

flow equations. The advantage of incorporating Darcy's Law into the Biot equations is that it permits use of parameters which are readily obtained from laboratory tests.

The flow through a flat duct of length ℓ under the pressure gradient $p_1 - p_2$ is pictured schematically in Figure 2.3. The height of the duct is 2a and a unit width of flow is considered. At an arbitrary distance, r, from the center of the duct, force equilibrium conditions can be established as

$$\gamma_f h_1 (2r) - \gamma_f h_2 (2r) + \mu \frac{dv}{dr} \cdot 2\ell = 0 \qquad (2\text{-}42)$$

where γ_f is the unit weight of fluid, h_1 and h_2 are the pressure heads at either end of the duct, μ is the dynamic viscosity and v is the fluid velocity at distance r. The first two terms of Equations 2-42 represent the pressure forces P_1 and P_2 acting on the area 2r at the left and right ends of the duct respectively. The last term is the viscous friction force acting along the two surfaces at a distance r from the centerline of the duct. Rearranging Equation 2-42 as

$$\gamma_f (h_1 - h_2) = -\mu \frac{dv}{dr} \frac{\ell}{r} \qquad (2\text{-}43)$$

and substitution of the hydraulic gradient i given by

$$i = \frac{h_1 - h_2}{\ell} \qquad (2\text{-}44)$$

into Equation 2-43 gives

$$dv = \frac{\gamma_f i}{\mu} r dr \qquad (2\text{-}45)$$

integrating both sides of Equation 2-45 from o to r gives the fluid velocity at the distance r as

$$v = -\frac{\gamma_f i}{2\mu} r^2 + C \qquad (2\text{-}46)$$

At the duct wall the fluid velocity must drop to zero and

$$C = \frac{\gamma_f i}{2\mu} a^2 \qquad (2\text{-}47)$$

Combining Equations 2-46 and 2-47 yields

$$v = \frac{\gamma_f i}{2\mu} (a^2 - r^2 \qquad (2\text{-}48)$$

The average velocity in the duct, V_a, is defined as

$$v_a = \frac{Q}{A} = \frac{1}{2a} \cdot 2 \int_o^a \cdot dr \qquad (2\text{-}49)$$

where Q is the total flow through the duct of area A (equal to 2a). Substitution of Equation 2-48 into the integral of 2-49 and manipulation gives

$$v_a = \frac{\gamma_f a^2}{3\mu} i \qquad (2\text{-}50)$$

This is the actual average fluid velocity relative to the duct. The duct represents only the pore volume of the soil. As explained in conjunction with Equation 2-5, the actual discharge velocity w_i, or apparent relative fluid velocity, is given by

$$\dot{w}_i = nv_a = \frac{na^2\gamma_f}{3\mu} \quad i \tag{2-51}$$

Darcy's Law states that

$$\dot{w}_i = ki \tag{2-52}$$

where k is the coefficient of permeability (cm/sec). From Equations 2-51 and 2-52 the coefficient of permeability for the flat duct can be expressed as

$$\boxed{k = \frac{na^2\gamma_f}{3\mu}} \tag{2-53}$$

A similar procedure can be followed for obtaining the average apparent flow velocity through a circular duct. This solution, known as the Hagen-Poiseulle flow law is given by

$$\dot{w}_i = \frac{na^2\gamma_f}{8\mu} i \tag{2-54}$$

where a is the radius of the circular duct (e.g. Bowles, 1979). From Equations 2-52 and 2-53 the coefficient of permeability for the circular duct is given as

$$k = \frac{na^2\gamma_f}{8\mu} \tag{2-55}$$

Biot's equations for viscous friction (2-39 and 2-41) can now be expressed in terms of the coefficient of permeability given in Equations 2-53 and 2-55. For the flat duct,

$$D_i = \frac{\gamma_f}{k}\dot{w}_i + \frac{\rho_f}{5n}\ddot{w}_i \tag{2-56}$$

and for the circular duct

$$D_i = \frac{\gamma_f}{k}\dot{w}_i + \frac{\rho_f}{3n}\ddot{w}_i \tag{2-57}$$

Note that in both of the above equations when the input excitation frequency drops to zero the last term drops out and Biot's equations agree exactly with Darcy's Law.

Explicit Form of Biot's Equations

The explicit friction force terms from Equations 2-56 and 2-57 for the flat and circular ducts can be substituted into Equation 2-10 for the pore pressure gradient giving

$$\pi_{,i} = \frac{\rho_f}{n}\left(1 + \frac{1}{5}\right)\ddot{w}_i + \rho_f\ddot{u}_i + \frac{\gamma_f}{k}\dot{w}_i \tag{2-58}$$

for the flat duct, and

$$\pi'_i = \frac{\rho_f}{n}\left(1 + \frac{1}{3}\right)\ddot{w}_i + \rho_f \ddot{u}_i + \frac{\gamma_f}{k}\dot{w}_i \qquad (2\text{-}59)$$

for the circular duct.

The inclusion of the explicit approximations for viscous friction in Equations 2-58 and 2-59 is in the form of a viscous shear given by Darcy's Law in the last term plus an added increment of inertial resistance associated with the apparent acceleration of the pore fluid relative to the skeleton. For the flat duct this increment is 1/5 and for the circular duct it is 1/3. The increment depends only on the pore shape and not the size.

As discussed previously in the subsection on Biot's equations, it was explained that the assumed flow paths in the form of flat and circular ducts were a poor approximation of the actual paths in saturated soil. In order to study the influence of more restrictive flow paths, Equations 2-58 and 2-59 can be generalized in the following form

$$\pi'_i = \frac{\rho_f}{n}(1 + r)\ddot{w}_i + \rho_f \ddot{u}_i + \frac{\gamma_f}{k}\dot{w}_i \qquad (2\text{-}60)$$

where r represents the additional inertia or mass increment factor which is a function of the flow path geometry.

TPDAP FORMULATIONS

The results of the previous analytic development are incorporated into the two phase finite element code TPDAP. Based on the governing differential equation for the bulk mixture

(Equation 2-7) and for the pore fluid (Equation 2-60), global equilibrium equations for two phase media are established. These global equilibrium equations are presented in discretized form in both the space and time domain. TPDAP uses either Newmark's β method or Wilson's θ method for time integration.

Notation

Positive signs are used for elongation and tension. A comma denotes differentiation with respect to the subsequent indices and a superposed dot denotes time rate.

σ_{ij} : total stress

σ'_{ij} : effective stress

π : pore fluid pressure

u_i : solid skeleton displacement

w_i : apparent fluid displacement relative to solid skeleton

ε_{ij} : solid skeleton strain

ε_v : solid skeleton volumetric strain

ε_f : fluid phase volumetric strain

$\{\bar{u}\}_e$: nodal solid skeleton displacement vector at the element degrees of freedom

$\{\bar{w}\}_e$: nodal apparent relative fluid displacement vector at the element degrees of freedom

$\{T\}$: applied boundary traction (total stress)

$\hat{\pi}$: specified boundary pore fluid pressure

$[q]$: inverse of permeability matrix

$[D^{ep}]$: elasto-plastic stress-strain matrix

n : porosity

K_w : bulk modulus of pore fluid

K_g : bulk modulus of solid grain

K_m : bulk modulus of soil/water mixture

ρ : bulk mass density of mixture

ρ_f : fluid mass density

β, γ : parameters of Newmark's β method

θ : parameter in Wilson's θ method

δ_{ij} : Kronecker's delta

$$\delta_{ij} = 0 \quad \text{if } i \neq j$$

$$\delta_{ij} = 1 \quad \text{if } i = j$$

Γ : mass increment factor

Field Equations in Two-Phase Dynamics

Effective stress strain relation:

By virtue of Terzaghi's effective stress law, the total stress is expressed as the sum of the effective stress and the pore water pressure

$$\sigma_{ij} = \sigma'_{ij} + \delta_{ij}\,\pi \qquad (2\text{-}61)$$

Strain-displacement relation:

Under the assumption of small displacement theory,

$$\varepsilon_{ij} = \frac{1}{2}\,(u_{i,j} + u_{j,i}) \qquad (2\text{-}62)$$

Continuity equation:

Based on the conservation of mass, the coupled continuity equation of flow, as derived by Kim (1982), is given by

$$d\pi = \left[(1 - n)\, d\varepsilon_v + n\, d\varepsilon_f \right] K_m \qquad (2\text{-}63)$$

where

$$K_m = \frac{K_g K_w}{K_w + n(K_g - K_w)} \qquad (2\text{-}64)$$

Solid skeleton constitutive law:

$$d\sigma'_{ij} = D^{ep}_{ijk\ell} d\varepsilon_{k\ell} \qquad (2\text{-}65)$$

Equation of motion for the bulk mixture:

The differential equation of motion governing the bulk mixture was derived earlier in this section and is expressed as follows:

$$\boxed{\sigma_{ij,j} = \rho \ddot{u}_i + \rho_f \ddot{w}_i} \qquad (2\text{-}7)$$

Equation of motion for the pore fluid:

The generalized form of Biot's equation was given by:

$$\boxed{\pi_{,i} = \frac{\rho_f}{n}(1 + r)\ddot{w}_i + \rho_f \ddot{u}_i + \frac{\gamma_f}{k}\dot{w}_i} \qquad (2\text{-}60)$$

Equation 2-60 was derived under the assumption of isotropic permeability. In an anisotropically permeable porous medium, the coefficient of isotropic permeability, k, can be replaced by the symmetric anisotropic permeability matrix, [k], given by Scheidegger (1957) as

$$[k] = \begin{bmatrix} k_{xx} & k_{xy} & k_{xz} \\ k_{xy} & k_{yy} & k_{yz} \\ k_{xz} & k_{yz} & k_{zz} \end{bmatrix} \qquad (2\text{-}66)$$

And the generalized form of Biot's equation in anisotropically permeable medium can be expressed as

$$\pi_{,i} = \frac{\rho_f}{n}(1 + r)\ \ddot{w}_i + \rho_f \ddot{u}_i + q_{ij}\ \dot{w}_i \qquad (2\text{-}67)$$

where

$$[q] = [k]^{-1}\ \gamma_f \qquad (2\text{-}68)$$

Discretized Global Equilibrium Equation

Two global equilibrium equations are derived, first in terms of field variables and then discretized by the nodal variables.

The first equation equates the total internal stresses plus the inertia forces to the applied boundary tractions. Letting the solid skeleton movement be the virtual displacement, δu, the following global equilibrium equation for the bulk mixture is established,

$$\int_v \{\delta\varepsilon\}^T\{\sigma\}dv = \int_s \{\delta u\}^T\{T\}ds - \int_v \{\delta u\}^T\ \rho\{\ddot{u}\}dv$$

$$- \int_v \{\delta u\}^T\ \rho_f\{\ddot{w}\}dv \qquad (2\text{-}69)$$

where $\delta\varepsilon$ is the virtual strain corresponding to the virtual displacement δu.

The second equation equates the applied pore pressure on the boundary to the internal pore pressure plus the flow resistance force plus the inertia force on the pore fluid. Taking the apparent relative fluid movement as the virtual displacement, δw, the internal virtual work done by the pore pressure should be equal to the external virtual work. That is,

$$\int_V (\delta W_{i,i})^T \pi dv = \int_V \{\delta w\}^T \hat{\pi} ds - \int_V \{\delta w\}^T [q]\{\dot{w}\} dv$$

$$- \int_V \{\delta w\}^T \rho_f \{\ddot{u}\} dv - \int_V \{\delta w\}^T \frac{(1 + r)}{n} \rho_f \{\ddot{w}\} dv \quad (2\text{-}70)$$

Field variables can be discretized into nodal values within the finite element.

$$\{u\} = [N]\ \{\bar{u}\}e$$

$$\{\varepsilon\} = [B]\ \{\bar{u}\}e$$

$$\{w\} = [N]\ \{\bar{w}\}e$$

$$w_{i,i} = \{1\}^T [B]\ \{\bar{w}\}e \quad (2\text{-}71)$$

where $\{1\}^T = < 1\ 1\ 1\ 0\ 0\ 0 >$

Replacing the field variables in Equations 2-69 and 2-70 by the discretized nodal variables using Equation 2-71 gives the following global equilibrium equations at time step n;

$$\begin{bmatrix} M_m & M_c \\ M_c^T & M_f \end{bmatrix} \begin{Bmatrix} \ddot{u}_n \\ \ddot{w}_n \end{Bmatrix} + \begin{bmatrix} O & O \\ O & H \end{bmatrix} \begin{Bmatrix} \dot{u}_n \\ \dot{w}_n \end{Bmatrix} + \begin{bmatrix} K_t + E & E \\ E^T & E \end{bmatrix} \begin{Bmatrix} \Delta\bar{u}_n \\ \Delta\bar{w}_n \end{Bmatrix}$$

$$= \begin{Bmatrix} F_n \\ G_n \end{Bmatrix} - \begin{Bmatrix} R^s{}_{n-1} + R^f{}_{n-1} \\ R^f{}_{n-1} \end{Bmatrix}$$

or

$$M \ddot{\bar{U}}_n + D \dot{\bar{U}}_n + K \Delta\bar{U}_n = P - R_{n-1} \qquad (2\text{-}72)$$

where

$$M_m = \Sigma \int_v [N]^T \rho [N] dv$$

$$M_c = \Sigma \int_v [N]^T \rho_f [N] dv$$

$$K_t = \Sigma \int_v [B]^T [D^{ep}] [B] dv$$

$$E = \Sigma \int_v [B]^T \{1\} K_m \{1\}^T [B] dv$$

$$R^s{}_{n-1} = \Sigma \int_v [B]^T \{\sigma'_{n-1}\} dv$$

$$R^f{}_{n-1} = \Sigma \int_v [B]^T \{1\} \pi_{n-1} dv$$

$$F_n = \Sigma \int_s [N]^T \{T\} ds$$

$$M_f = \Sigma \int_v [N]^T \frac{(1+r)}{n} \rho_f [N] dv$$

$$H = \Sigma \int_v [N]^T [q][N] dv$$

$$G_n = \Sigma \int_v [N]^T \hat{\pi}_n \, ds$$

Now introducing Newmark's β method and Wilson's θ method for time integration, Equation 2-72 can be expressed in the following form;

$$\tilde{K}_t \, \Delta\tilde{U}_n = \tilde{P}_n \qquad (2\text{-}73)$$

where

$$\tilde{K}_t = K + \frac{1}{\beta\tau^2} M + \frac{\gamma}{\beta\tau} D \qquad (2\text{-}74)$$

and

$$\tilde{P}_n = P_n - R_{n-1} + \frac{1}{\beta\tau^2} M \left(\tau \dot{\bar{U}}_{n-1} + \left(\frac{1}{2} - \beta \right) \tau^2 \ddot{\bar{U}}_{n-1} \right)$$

$$+ \frac{\gamma}{\beta\tau} D \left(\left(1 - \frac{\beta}{\gamma} \right) \tau \dot{\bar{U}}_{n-1} + \left(\frac{1}{2} - \frac{\beta}{\gamma} \right) \tau^2 \ddot{\bar{U}}_{n-1} \right) \qquad (2\text{-}75)$$

with

$$\tau = \theta \, \Delta t \qquad (2\text{-}76)$$

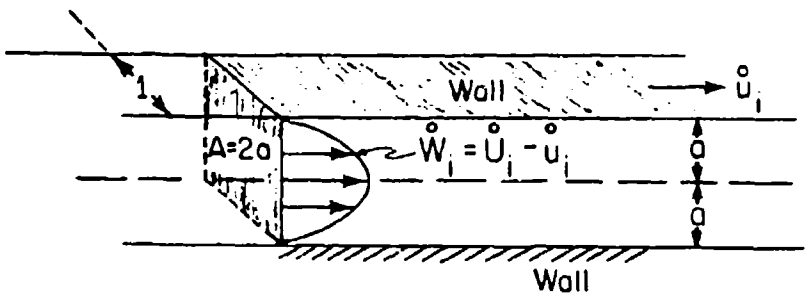

Figure 2.1. Schematic view of fluid flow in a flat duct

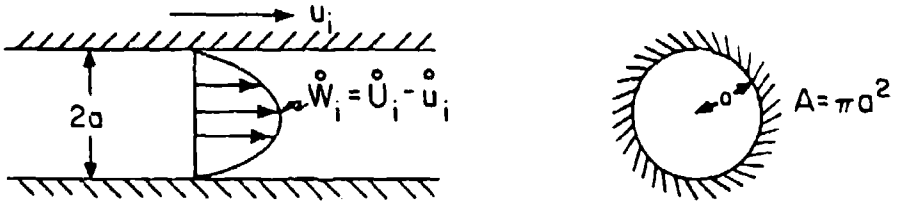

Figure 2.2. Schematic view of fluid flow in a circular duct

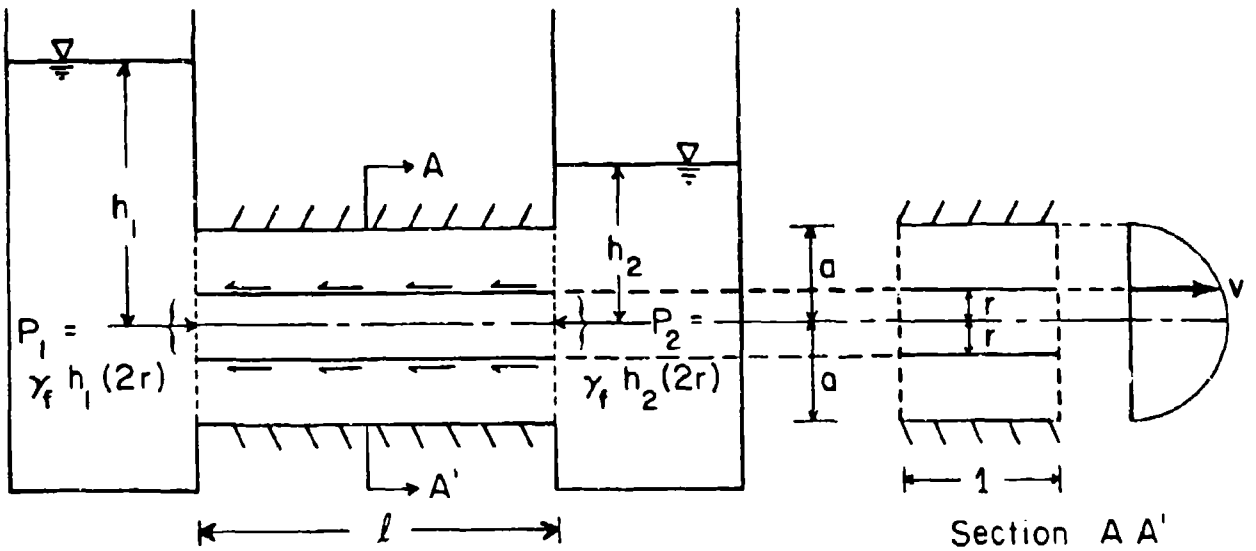

Figure 2.3. Force equilibrium in fluid flow through a flat duct

SECTION 3

TWO PHASE DYNAMIC ANALYSIS -

SATURATED POROUS ELASTIC SKELETON

INTRODUCTION

The next two sections present a series of parameter studies in which saturated two phase porous materials are subjected to dynamic uniaxial loadings. These parametric calculations, using the TPDAP code, were arranged so that the influence of the various material and loading parameters on the overall response could be isolated and analyzed individually. Three different soil skeletons were modeled. In this section a linear elastic skeleton was studied. In the following section a bilinear hysteretic skeleton was modeled, followed by calculations on an actual sand from Enewetak Atoll.

In this section three different loadings are applied; a step (or Heaviside) loading pulse, a triangular loading, and a fifth order simple polynomial loading. All loadings applied a peak stress of 5 ksi. Other parameters investigated in the elastic calculations include a comparison between two phase and total stress (one phase) analysis, the influence of mass discretization techniques, the influence of Biot's additional inertia term, and the influence of permeability, numerical damping, and surface drainage conditions.

CALCULATIONAL AND MATERIAL PARAMETERS

Loading Functions

The three 5 ksi loading time histories used in this section are shown in Figure 3.1. The rise time for all loadings was 0.1 msec. The triangular and polynomial loadings had a positive phase duration of 20.1 msec. The pressure decay of polynomial loading is given by

$$p(t) = p_o \left(1 - \frac{(t - t_r)}{t_o} \right)^5 \qquad (3\text{-}1)$$

where p_o is the peak pressure, t the time, t_r the rise time, and t_o the decay time. The total impulse under the polynomial loading is one third of the impulse under the triangular loading.

Finite Element Parameters

All the calculations throughout this study used the finite element mesh shown in Figure 3.2. The mesh consists of 200 elements with a total depth of 100 ft. The elements increase in thickness with increasing depth, starting with a thickness of 0.2 ft at the loading surface and expanding to 0.8 ft at the 100 ft depth. A constant time step of 0.05 msec was used in all calculations.

A number of parameters were standardized for the calculations in this section. These were held constant in most of the calculations, except when the influence of varying any one of these parameters was examined. The most suitable value of

each parameter was not known beforehand; thus, the sensitivity to each was examined as part of this parameter study.

In most calculations, the loading pressure function was partitioned on the ground surface in proportion to the areal ratio of the solid and fluid constituents. In other words, n% of the total force on the loading boundary was applied to the pore water and the remaining (1 - n)% was applied to the soil skeleton. For the porosity of 35% and peak stress of 5 ksi, the peak stress applied to the pore water at the loading boundary was 1750 psi while the peak effective stress applied to the soil skeleton was 3250 psi.

In the discussion of Biot's equations of Section 2, an additional inertia term (Equation 2-60) was added to TPDAP to account for the increased friction forces which develop at higher frequencies. In most of the calculations in this section, r is given a value of zero; i.e. there is no added friction force due to relative acceleration between the skeleton and pore fluid. The only friction force between the two is proportional to the relative velocity and is given by Darcy's law.

For high frequency loadings, such as used in this study, oftentimes oscillations develop at the wavefront. To minimize the potential for oscillations, numerical damping was introduced into most calculations in this section. In this study Newmark's method for time integration was selected, with $\gamma = 1.2$, which results in relatively heavy damping. The corresponding value of $\beta = 0.7225$ calculated from

$$\beta = \frac{(\gamma + 0.5)^2}{4} \qquad (3\text{-}2)$$

was used.

Archer (1963) demonstrated that the conventional lumped treatment of mass in finite element calculations can result in large errors when significant inertial forces are present. More accurate solutions can be obtained by use of the consistent mass matrix technique described by Archer, in which the matrix is consistent with the actual distribution of mass in the medium. The use of the consistent mass technique results in a symmetric mass matrix rather than the simple diagonal mass matrix of the lumped mass approach. In most of the calculations in this study the consistent mass technique is used.

Material Parameters

The material properties used in the linear elastic analysis are summarized in Table 3.1. The skeleton properties are representative of a uniform medium dense uncemented quartz sand. The elastic moduli, From Blouin and Kim (February, 1984) are the secant moduli at 1.5% strain, obtained from laboratory data on 5 typical sands. The undrained bulk modulus of the soil water mixture, K_m, is obtained from the Wood equation and represents the modulus of the soil water mixture with no stiffness contribution from the soil skeleton (for further discussion see Blouin and Kim, February 1984 and Richart et al., 1970). Based on the Wood equation, a compressional wavespeed of 5161 ft/sec is computed.

The simplest model for the composite undrained compressibility of the saturated soil is the decoupled model (Blouin and Kim, February, 1984). The decoupled model assumes that the stress is resisted by the stiffness of the soil skeleton acting in parallel with the stiffness of the soil-water mixture from the Wood equation. The resultant bulk and constrained moduli, K_d and M_d, are simply the sum of the mixture modulus and the bulk and constrained moduli of the soil skeleton respectively. In the undrained case, the TPDAP continuity

equation combined with Terzaghi's effective stress law results in the decoupled modulus equations.

Transmitting Boundary

In order to prolong the calculation time available with the mesh of Figure 3.2, a transmitting boundary was employed on the base of the bottom element. In establishing this boundary, it was assumed that there was no relative motion between the pore fluid and solid skeleton at the boundary. This condition is expressed as

$$w_i = 0 \tag{3-3}$$

where w_i is the apparent fluid displacement relative to the soil skeleton at the boundary. Thus, the saturated soil is assumed to have no drainage at the boundary and the equations for the undrained decoupled modulus of Table 3.1 apply. This implies that beneath the boundary one phase total stress analysis is valid, where the compressional wavespeed

$$C_{pd} = \sqrt{\frac{M_d}{\rho}} \tag{3-4}$$

from Table 3.1 is used.

The above assumptions permit use of the transmitting boundary developed by Lysmer and Kuhlemeyer (1969) where the stress wave energy on the boundary is absorbed by dashpots at the element nodes. The total normal stress on the boundary, σ_n, is given by

$$\sigma_n = \rho C_{pd} \dot{u}_n \tag{3-5}$$

where $\dot{u}_n$ is the absolute velocity of the skeleton normal to the boundary. In order for the energy dissipated in the dashpots to just equal the energy in the compressional wave, the dashpot constants are proportional to the undrained impedence ρC_{pd}.

Because there is relative motion between the skeleton and the pore fluid, the above assumptions do not entirely eliminate reflections from the boundary. Development of truly non-reflecting boundaries for two phase media is beyond the scope of this work. However, use of the above assumptions in the elastic two phase calculations greatly reduced reflections from the boundary.

HEAVISIDE LOADING

The Heaviside loading from Figure 3.1 was used in the initial series of parametric calculations because it represented a simple loading and permitted study of pore pressure dissipation toward the ground surface.

One Phase Calculations

Two conventional one phase calculations were performed under the Heaviside loading with mass discretization using the consistent and lumped techniques. These are compared in Figure 3.3 in the form of pore pressure profiles at times of 2, 6, and 10 msec. The material properties from Table 3.1 were used, with the moduli given by the undrained decoupled moduli, K_d and M_d. The results of the one phase total stress calculations were converted to pore pressure for comparison to the pore pressure profiles obtained in the later two phase calculations.

The total vertical stress, σ_v, in uniaxial loading is given by

$$\sigma_v = M_d \varepsilon_v \qquad (3\text{-}6)$$

where ε_v is the vertical strain and M_d is the decoupled constrained modulus from Table 3.1. As described by Blouin and Kim (February, 1984), the effective stress, σ_v', in uniaxial loading is given by

$$\sigma_v' = M_s \varepsilon_v \qquad (3\text{-}7)$$

where M_s is the constrained modulus of the skeleton. According to Terzaghi's effective stress law, the total stress is comprised of the effective stress plus the pore water pressure, π, as

$$\sigma_v = \pi + \sigma_v' \qquad (3\text{-}8)$$

The ratio of the pore pressure to the total vertical stress in an undrained uniaxial loading is obtained by solving Equation 3-8 for π and substituting the values of total and effective stress from Equations 3-6 and 3-7 into the ratio to give

$$\frac{\pi}{\sigma_v} = \frac{M_d - M_s}{M_d} \qquad (3\text{-}9)$$

Using the values of M_d and M_s from Table 3.1 gives the ratio as

$$\frac{\pi}{\sigma_v} = 0.892 \qquad (3\text{-}10)$$

Thus, the pore pressure profiles of Figure 3.3 were obtained by multiplying the total vertical stress from the one phase calculations by the ratio of pore pressure to total stress given in Equation 3-10.

As demonstrated in Figure 3.3, there is no significant difference between the one phase calculations using the lumped mass technique and those using the consistent mass technique. Because the mesh used in these calculations is so fine, the errors introduced by the lump mass technique into the one phase calculation are negligible.

TWO PHASE CALCULATIONS

Lumped Mass vs. Consistent Mass Calculations

The initial set of two phase calculations under the Heaviside loading compared the computed response using the lumped mass technique with that of the consistent mass technique. In contrast to the one phase results, there was a significant difference between the two techniques in the two phase calculations. This difference is illustrated in the stress profile comparisons at 2, 6, 10 and 14 msec shown in Figure 3.4.

As discussed previously, the 5 ksi Heaviside loading is applied at the surface and is partitioned between the soil skeleton and the pore water at the loading boundary. For the assumed porosity, 35% or 1750 psi is applied to the pore water

and the remaining 65% or 3250 psi is applied to the solid skeleton. Despite this partitioning at the surface, Figure 3.4 shows that within several feet from the surface the load is redistributed between the two phases so that the pore water carries about 90% of the total load, as specified by Equation 3-10 for the undrained condition. Because of the fluid friction between the pore water and the skeleton, the stress distribution applied at the surface is very rapidly transformed to that which would result from an undrained loading.

The permeability of the soil skeleton permits flow of pore water toward the surface. This flow results from the pore pressure gradient between the high pressure in the undrained region behind the wavefront and the 1750 psi pore pressure applied at the ground surface. The pore water migration from the high pressure region toward the low pressure boundary region causes dissipation of the pore pressure. As the pore pressure decreases, the intergranular or effective stress increases as the skeleton compresses and assumes an increasing portion of the total stress. At all depths, the sum of the pore pressure and the effective stress equals the total stress. The pore pressure dissipation advances downward from the surface with increasing time. The rate of advancement is a function of the permeability and the pore pressure gradient as in the usual consolidation process. At 14 msec, the pore pressure dissipation front has reached a depth of about 15 ft.

At the wavefront in Fiure 3.4, the profile computed using the lumped mass matrix is considerably more smeared than that computed from the consistent mass matrix. In Equation 2-72 the first matrix multiplication term

$$\begin{bmatrix} M_m & M_c \\ M^T_c & M_f \end{bmatrix} \begin{Bmatrix} \ddot{u}_n \\ \ddot{w}_n \end{Bmatrix}$$

expresses the inertial resistance of the bulk mixture and the pore water. The inertial force vector for the soil water mixture $\{I_m\}$ is given by

$$\{I_m\} = [M_m]\{\ddot{u}_n\} + [M_c]\{\ddot{w}_n\} \qquad (3\text{-}11)$$

and the inertial force vector for the pore fluid $\{I_f\}$ is given by

$$\{I_f\} = [M_c]^T\{\ddot{u}_n\} + [M_f]\{\ddot{w}_n\} \qquad (3\text{-}12)$$

The consistent mass matrix includes all the mass (M) terms in the above matrix. However, the lumped mass matrix includes only the M_m and M_f terms in the above matrix. In addition, the lumped mass matrices M_m and M_f are diagonalized, which introduces an additional error. The effect of neglecting the coupling mass matrix term, M_c, drops the second inertial force term out of Equation 3-11 and the first inertial force term out of Equation 3-12. In most problems the acceleration of the skeleton, $\ddot{u}_n$, is much greater than the relative acceleration between the pore fluid and the skeleton, $\ddot{w}_n$. In Equation 3-11, the coupling mass matrix, M_c, is also smaller than the mass matrix for the mixture, M_m. Thus, the second inertial force term is of relatively minor importance. However, in Equation 3-12 the coupling mass matrix is associated with the relatively large skeleton acceleration; and the contribution of this term is substantial.

The first inertial force term in Equation 3-12 corresponds to the second inertial force term, $\rho_f\ddot{u}_i$, in the governing differential equation of motion of the pore fluid, Equation 2-60. Inspection of Equation 2-60 shows that neglecting

this term will significantly increase the apparent relative velocity and acceleration, $\dot{w}_i$ and $\ddot{w}_i$, for a given pore pressure gradient. This increased relative motion will result in unrealistically high energy dissipation and smearing of the wavefront as shown in Figure 3.4. In general, the lumped mass technique is inappropriate for use in two phase dynamic analysis.

Comparison of One and Two Phase Calculations

The pore pressure profiles from the one phase calculation using the consistent mass matrix are compared to those from the two phase calculation in Figure 3.5. The pore pressure dissipation near the surface in the two phase calculation is clearly evident. At the wavefront the two phase calculation is smeared considerably; however, this is not a result of numerical smearing but is due to the dissipation of energy near the front resulting from the relative motions induced between the pore water and soil skeleton. The effect is similar to that caused by numerical damping, but in this case is a real physical effect.

Influence of Mass Increment Factor

The final parameter examined in the Heaviside loading calculations was the influence of the mass increment factor, r, included in Equation 2-60. As explained in Section 2, r is a factor which attempts to account for frictional resistance between the pore fluid and skeleton in excess of the resistance accounted for by Darcy's law. For Biot's evaluation of the circular and flat ducts, the factor r depends on the shape of the duct but is independent of the size. The value of r for the circular duct is 1/3 and the value for the flat duct is 1/5.

Figure 3.6 compares pore pressure and effective stress profiles for two phase calculations with r equal to zero and r equal to 1/3. For an r of 1/3 there is a slight reduction in the smearing at the wavefront. The additional frictional

resistance due to the r factor results in somewhat reduced relative motion and energy dissipation; a trend toward less smearing of the wavefront as seen in the undrained one phase calculation. As noted in the discussion of Section 2, the actual pore shapes are far more complicated than the simple models used by Biot, so realistic values of r may be much greater than those he derived. This is an area requiring further research.

TRIANGULAR LOADING

One Phase vs. Two Phase Calculations

The triangular loading function of Figure 3.1 was used in a second series of parametric calculations. With a rise time of 0.1 msec and a positive phase duration of 20.1 msec, this pressure function more nearly approximates certain airblast loadings. The first series of calculations using the triangular loading pulse compared the pore pressure response from one and two phase calculations as shown in Figure 3.7. In the one phase calculation, plotted as a dashed line, the pore pressure rises rapidly to a peak which is followed by a linear decay which mirrors the linear decay of the loading waveform. As explained in conjunction with the one phase calculation for the Heaviside loading, the pore pressure is obtained by multiplying the total stress by 0.892 given by Equation 3-9. The solid line shows the profiles from the two phase calculation. At the wavefront, there is significant smearing compared to the one phase calculation and some attenuation of the peak stress. Both the smearing and additional peak stress attenuation are primarily due to the energy dissipation associated with the relative motion between the pore fluid and the skeleton. Note that there is also some attenuation of the peak stress in the one phase profile as the wave propagates downward. At the surface the applied peak stress is 4460 psi. At 14 msec and a depth of 68 ft, the peak stress has attenuated by 9% to about 4060 psi. This stress attenuation

in the one phase calculation is due to the numerical damping. The additional peak stress attenuation in the two phase calculation is due to dissipation by fluid friction. At 14 msec in the two phase calculation the peak stress has attenuated by an additional 9% to a value of 3660 psi at a depth of 64 ft.

In the near surface region the two phase calculation shows a decrease in pore pressure resulting from partial drainage toward the surface. At 14 msecs the pore pressure dissipation front has reached a depth of 13 ft, slightly less than that observed for the Heaviside loading. This slower dissipation front is due to the smaller pore pressure gradients under the triangular loading.

Influence of Permeability

The second parameter examined in the series of triangular loading calculations was the influence of permeability on the material response. Figure 3.8 compares the pore pressure and effective stress profiles at various times between a soil having the standard 0.1 in/sec permeability and a soil having a permeability of 0.001 in/sec. The higher permeability is typical of a coarse uniform sand of high permeability while the lower value is typical of well graded sands of medium permeability. There are significant differences between the two calculations both at the wavefront and in the near surface region. As expected, pore pressure dissipation toward the surface is severely curtailed in the lower permeability material. At 14 msec the pore pressure dissipation front has reached a depth of less than 2 ft, compared to about 13 ft in the more permeable soil.

The wavefront in the lower permeability soil is significantly less smeared than that in the higher permeability soil. The lower permeability inhibits relative motion between the pore fluid and soil skeleton at the wavefront, thus, lessening the energy dissipation effects due to fluid friction.

Comparing the profiles for the two phase calculation in the low permeability soil to the one phase calculation plotted in Figure 3.7 shows that the two phase calculation is nearly identical to the one phase undrained case. Under the one dimensional linear elastic assumptions of this set of calculations, the one phase calculation adequately models the response of this medium permeability soil to the dynamic loading.

Influence of Mass Increment Factor

The third parameter investigated in this series of calculations was the influence of the mass increment factor r. Under the Heaviside loading, use of an r value of 1/3, corresponding to Biot's circular pores, had only a small influence on the response at the wavefront (see Figure 3.6). Figure 3.9 compares the effective stress and pore pressure profiles for calculations using r values of zero and one. An r value of one was picked to accentuate the influence of r. There is less smearing of the wavefront for the calculation using an r of one, the difference being considerably greater than in the previous comparison using an r value of 1/3. As was mentioned previously, increasing the r value results in effectively increasing inertial resistance in the pore fluid while reducing the relative fluid motions. However, it is not known whether an r of one is a meaningful value for this parameter.

Influence of Damping

The next parameter studied in the triangular loading series was the influence of the γ damping on the response of the two phase material. A rather heavy γ damping of 1.2 was used as the standard throughout most of this study. Figure 3.10 compares the pore pressure and effective stress profiles calculated using the standard damping and no γ damping, i.e. $\gamma = 0.5$. Behind the

peak stresses, the two solutions are identical. At the wavefront, the undamped profile exhibits a sharp jump in pore pressure, as compared to the more smeared increase in pressure in the damped case. At early time, the undamped stresses exhibit oscillations just behind the wavefront. Beyond 10 msec (below a depth of 60 ft), these oscillations no longer occur. Finally, the smearing around the peak stress in the damped calculation is duplicated in the undamped calculation, indicating that it is indeed caused by the dissipation resulting from relative motion between the two phases near the wavefront and is not associated with numerical damping.

Another comparison of the influence of damping is illustrated in Figure 3.11 where the standard damping with γ = 1.2 is compared to the response for a damping of 0.85, midway between the previous comparisons. There is little difference between these two calculations. The 0.85 damping exhibits slightly less smearing at the wavefront. In retrospect, very little damping would have been required in the linear elastic analysis. However, hysteretic materials normally exhibit more severe oscillations due to changes in material properties. In such calculations heavier damping may be preferable.

Influence of Mass Discretization Technique

The effect of using the lumped mass technique in a two phase triangular loading calculation is demonstrated in Figure 3.12. The results are similar to those for the Heaviside loading which were discussed in detail in conjunction with Figure 3.4. Use of the lumped mass technique causes heavy smearing in the vicinity of the wavefront and is not suitable for use in these two phase calculations (refer to the previous discussion for more details).

Influence of Surface Drainage Conditions

The sixth and final parameter investigated using the triangular loading function is the influence of the surface drainage conditions on the stress profiles. In the first portion of this phase of the study, the triangular loading function was applied with no drainage allowed at the ground surface. This calculation is compared to th. standard case in Figure 3.13 where drainage is only partially inhibited by the specified pore pressure loading (i.e. the pore pressure equals 35% of the total applied load). The profiles for the calculations with no surface drainage are plotted as dashed lines. This calculation was performed by prohibiting relative motion between the pore water and skeleton at the loading surface while applying the total load to the ground surface. At the ground surface, the pore pressure at the impermeable boundary is much higher than that on the partially drained boundary. Though the pore pressure builds up very rapidly as the wavefront moves away from the partially drained boundary, the buildup does not quite reach the magnitude of the pore pressure developed beneath t.e impermeable boundary. Thus, the pore pressures near the peak are slightly higher in the case of the impermeable loading boundary. Because of the impermeable boundary, there is no pore pressure dissipation in the near surface region in that calculation.

Comparison of the two phase calculation on the impermeable loading boundary of Figure 3.13 with the totally undrained one phase calculation of Figure 3.7 shows that in the near surface region the pore pressure response in both calculations is nearly identical. At greater depths, however, the response of the two phase calculation near the wavefront matches that of the drained two phase calculations.

Figure 3.14 shows a comparison between the pore pressure and effective stress profiles for partially drained and fully drained conditions at the loading boundary. In the partially

drained standard calculation, 35% of the total load is applied to the pore water. In the fully drained calculations, the total load is applied on the soil skeleton, thus maintaining zero pore pressure at the loading boundary. In both calculations, the pore pressures increase very rapidly with depth and are nearly equal at the wavefront at all the times shown.

It is concluded from the results of the calculations shown in Figures 3.13 and 3.14 that wave propagation in two phase media is quite independent of the loading and/or drainage conditions assumed at the ground surface. This is a fortunate effect because the actual partitioning of the loading pressure between the pore water and the soil skeleton on the surface is difficult to assess.

POLYNOMIAL LOADING

Two parametric calculations were performed using the linear elastic properties of Table 3.1 and the simple fifth order polynomial pressure loading shown in Figure 3.1 The loading has a 0.1 msec risetime and a decay described by

$$p(t) = p_o \left(1 - \frac{(t - t_r)}{t_o} \right)^m \qquad (3\text{-}13)$$

where the peak pressure, p_o, is 5 ksi, t is the time, t_r the rise time, the decay time, t_o, is 20 msec, and the decay exponent, m, is 5. This loading function closely approximates many explosively generated airblast loadings with their rapid early time pressure decay. As noted previously, the impulse under the fifth order loading is 1/3 of the impulse under the triangular loading used in the previous set of parametric calculations.

One Phase vs. Two Phase Calculations

Results of one and two phase calculations using the fifth order polynomial loading are compared in Figure 3.15. As in the previous studies, the one phase total stress is multiplied by 0.892 from Equation 3.10 to obtain the pore pressure under the assumption of no drainage. The two phase calculation used the standard load partitioning, with 35% of the total pressure (1750 psi) applied to the pore water. Attenuation of the sharp peak in the polynomial pressure loading function is more rapid than that observed for the triangular loading. At 14 msec the peak pore pressure from the one phase calculation has decayed from 4460 psi at the surface to 3180 psi at the 70 ft depth, a decrease of nearly 29%. This is much larger than the 9% drop observed in the corresponding triangular loading calculation. The greater attenuation is due to numerical damping of the much steeper pressure decay from the peak. Use of less γ damping would have minimized this attenuation.

The two phase pore pressure profile, shown as a solid line in Figure 3.15, is significantly more smeared and attenuated than the one phase pore pressure profile. This is similar to the effects observed in both the Heaviside and triangular loading cases. The peak pore pressure in the two phase calculation at 14 msec is only 2500 psi, 44% less than the surface peak pore pressure. The additional 15% drop in pressure is due to the fluid damping associated with the relative motion between the pore water and the soil skeleton. In the triangular loading calculations, the additional attenuation due to the fluid damping was 9%. The difference indicates that the fluid damping is sensitive to the frequency of the loading function, being more severe for steeper pressure gradients.

Polynomial vs. Triangular Loadings

Figure 3.16 compares the pore pressure and effective stress profiles from the standard two phase calculations under the polynomial and triangular loadings. The initial rises in pore pressure and effective stress are identical in the two calculations. However, the more severe numerical and fluid damping cause both the pore pressure and effective stress under the polynomial loading to attenuate more rapidly than those under the triangular loading. The shape of the loading functions and the attenuation characteristics result in an apparently more rapid propagation of peak stress under the polynomial loading than under the triangular loading. At 14 msec the peak stress is at a depth of 70 ft under the polynomial loading but has reached a depth of only 63 ft under the triangular loading.

Table 3.1. Material parameters used in linear elastic calculations.

MATERIAL PROPERTIES

(typical values)

Porosity

$n = 0.35$

Specific gravity of solid grains (quartz)

$G_s = 2.67$

Permeability

$k = 0.1$ in/sec

Unit Weight

Pore water $\gamma_w = 62.4$ lb/ft^3

Bulk mixture $\gamma_t = 130.1$ lb/ft^3

Modulus

Skeleton bulk modulus	$K_s = 50{,}111$ psi
Skeleton shear modulus	$G_s = 30{,}067$ psi
Skeleton constrained modulus	$M_s = 90{,}200$ psi
Skeleton Poisson's ratio	$\nu_s = 0.25$
Water bulk modulus	$K_w = 0.29 \times 10^6$ psi
Solid grain bulk modulus	$K_g = 5 \times 10^6$ psi
Mixture undrained bulk modulus (Wood equation)	$K_m = \dfrac{K_g K_w}{K_w + n(K_g - K_w)} = 0.748 \times 10^6$ psi
Decoupled undrained bulk modulus	$K_d = K_m + K_s = 0.798 \times 10^6$ psi
Decoupled undrained constrained modulus	$M_d = K_m + M_s = 0.838 \times 10^6$ psi

Table 3.1. Material parameters used in linear elastic calculations (concluded).

P-wave Speed

Water	$c_{pw} = 4641$ ft/sec
Skeleton	$c_{ps} = 1583$ ft/sec
Mixture (undrained)	$c_{pm} = \sqrt{\frac{K_m}{\rho}} = 5161$ ft/sec
Decoupled (undrained)	$c_{pd} = \sqrt{\frac{M_d}{\rho}} = 5463$ ft/sec

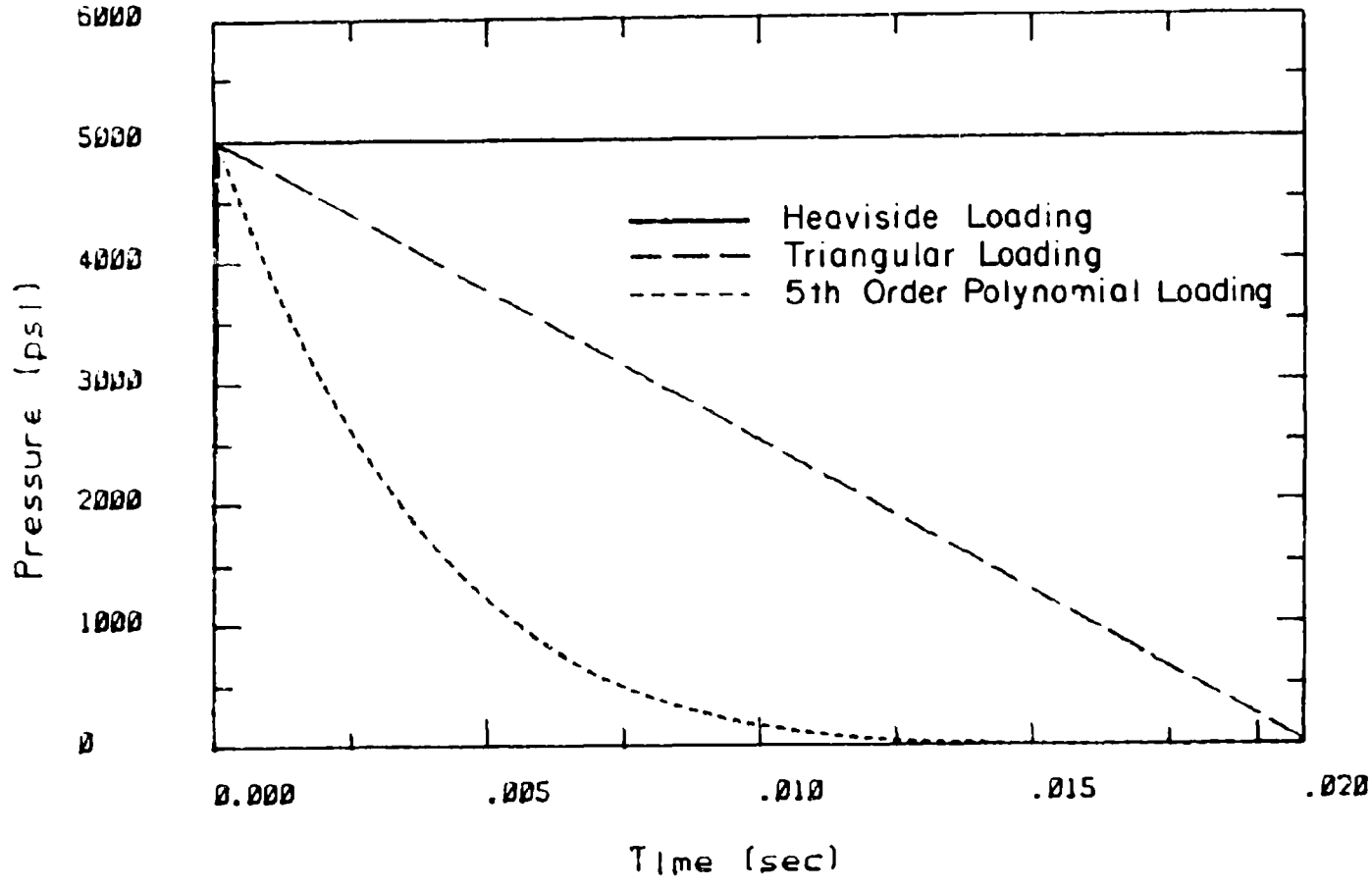

Figure 3.1. Surface loading pressure functions

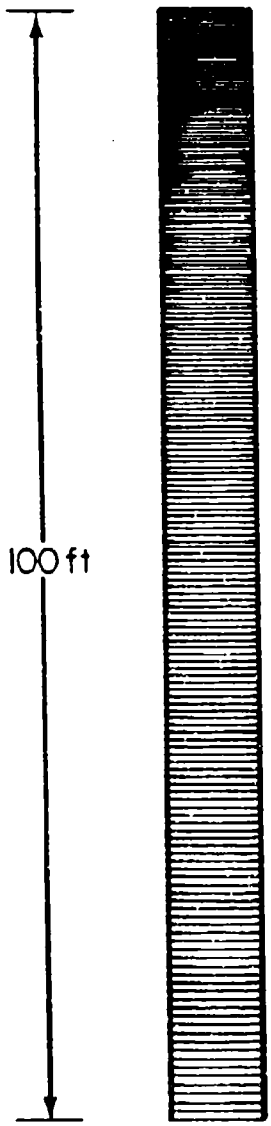

Figure 3.2. Finite element mesh

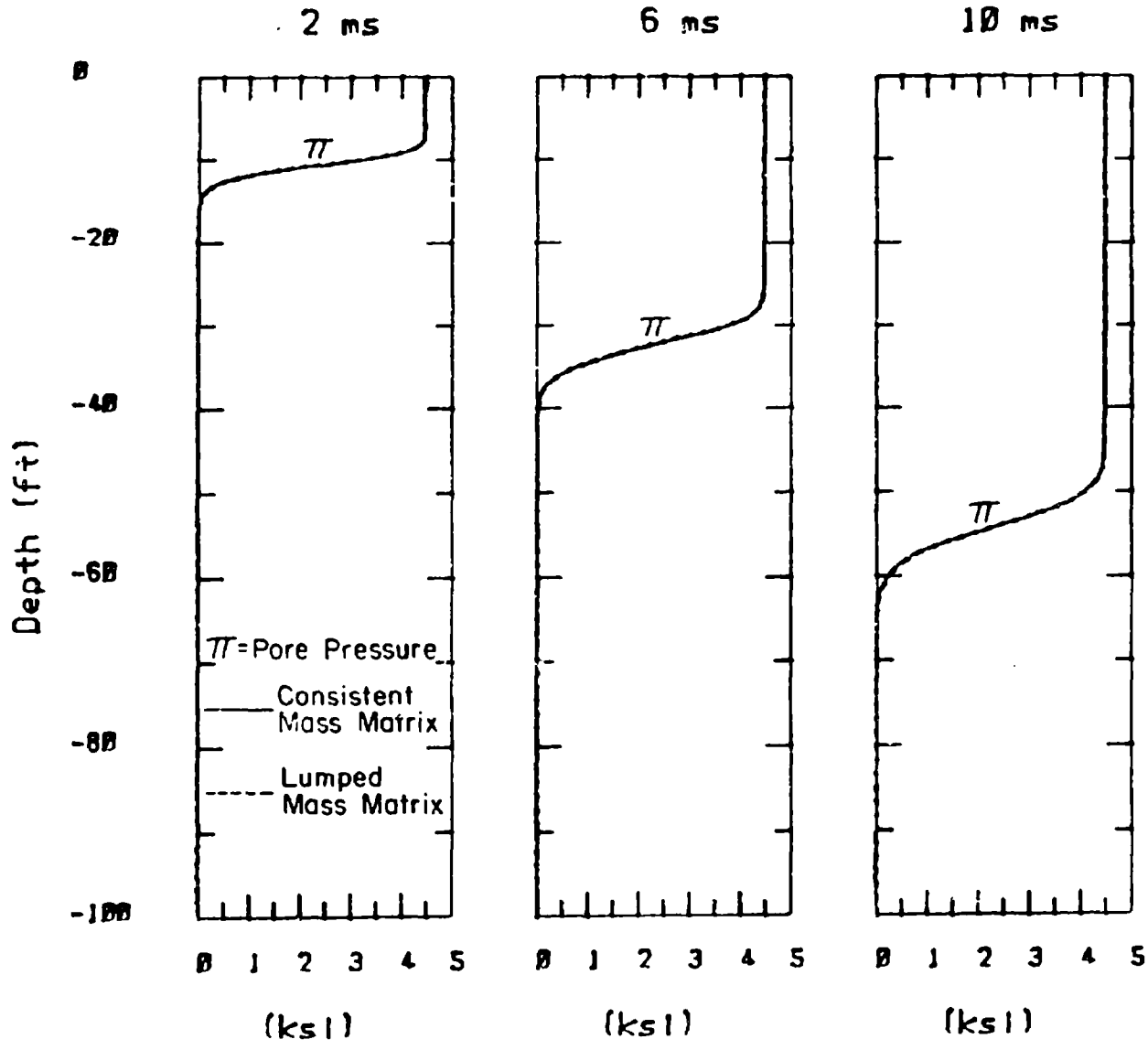

Figure 3.3. Pore pressure profiles from one phase calculations using consistent and lumped mass matrices

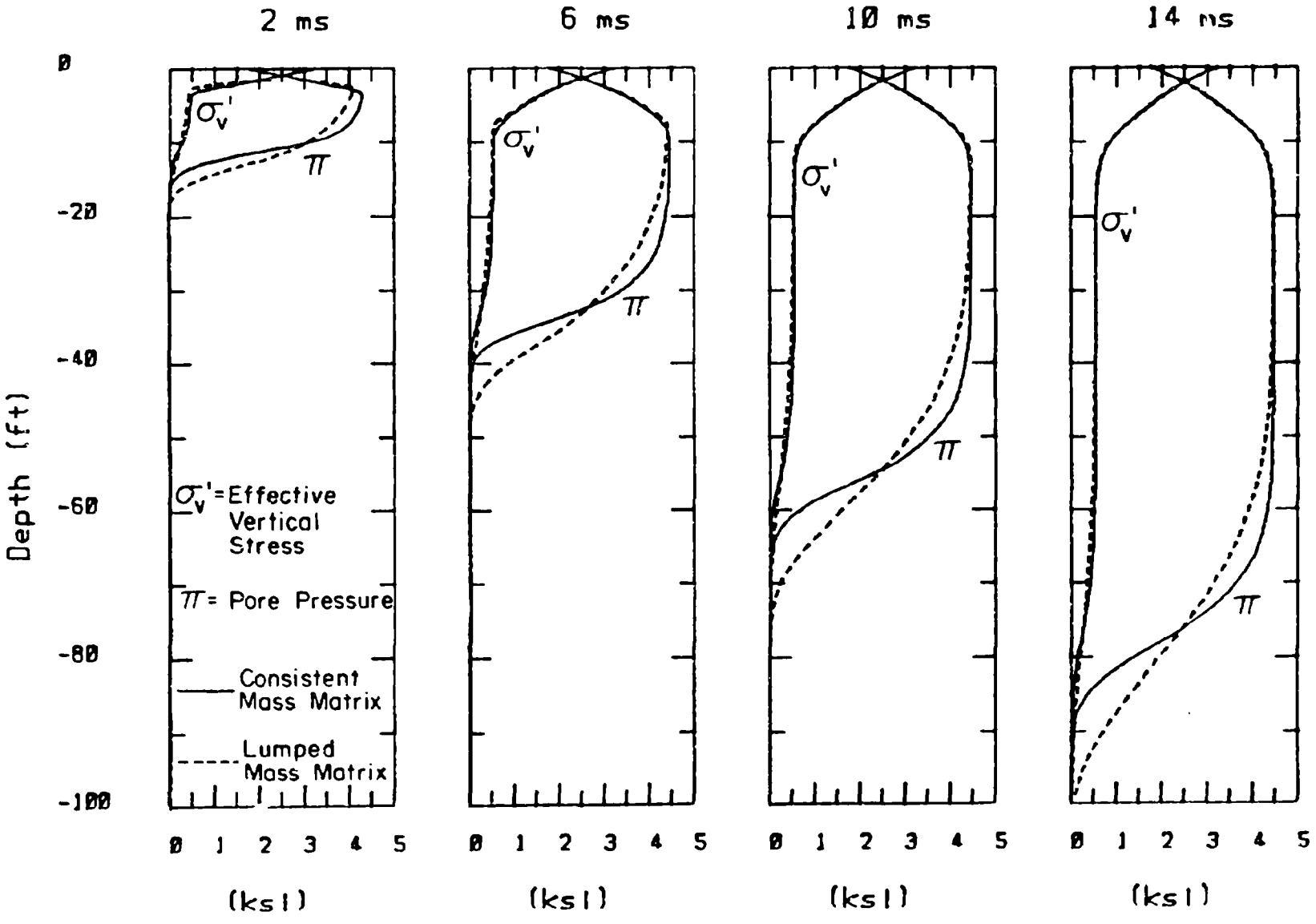

Figure 3.4. Stress profiles from two phase calculations using consistent and lumped mass matrices, Heaviside loading

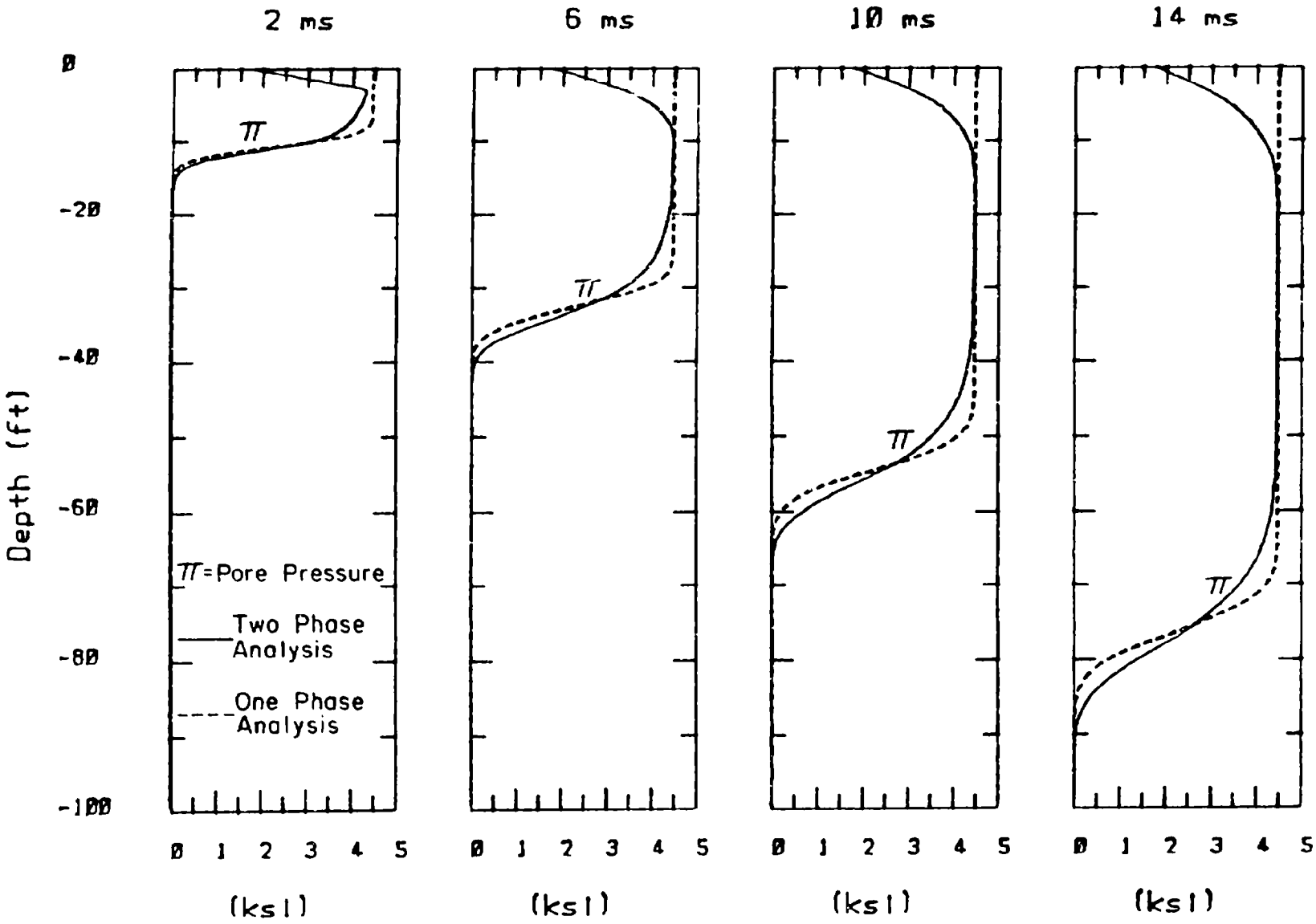

Figure 3.5. Comparison of pore pressure profiles from one and two phase calculations, Heaviside loading

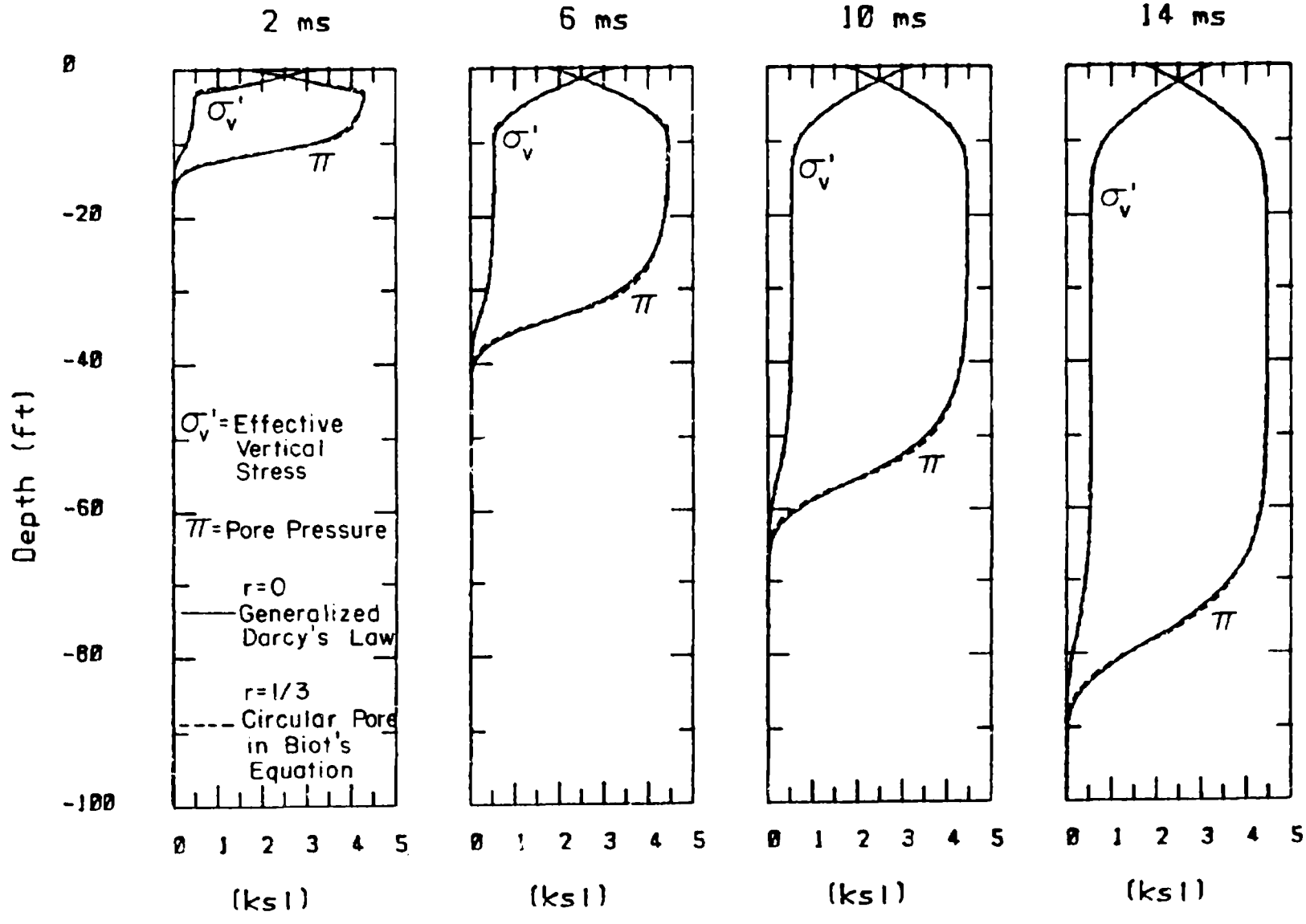

Figure 3.6. Influence of mass increment factor, r, on stress profiles, Heaviside loading

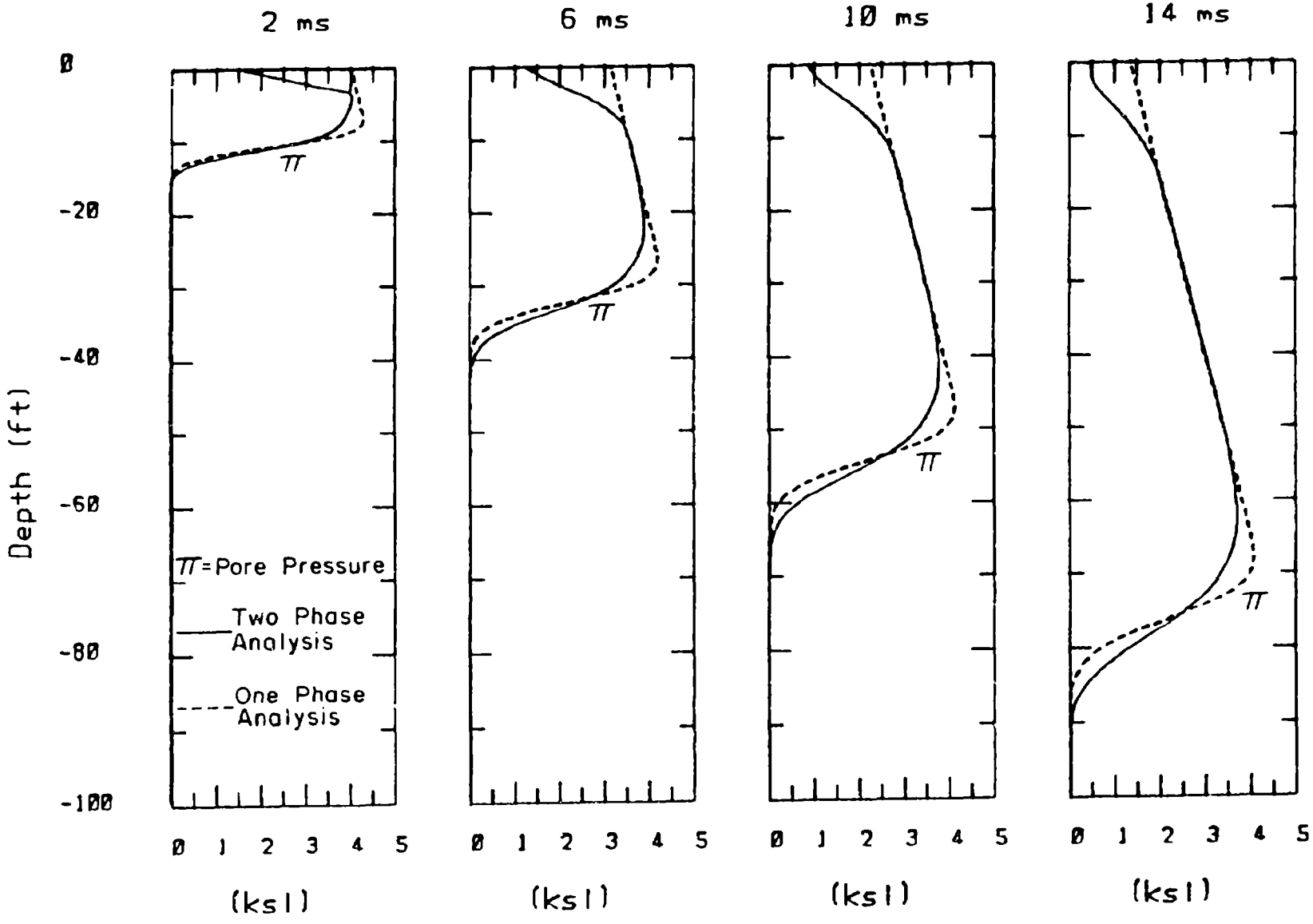

Figure 3.7. Comparison of pore pressure profiles from one and two phase calculations, triangular loading

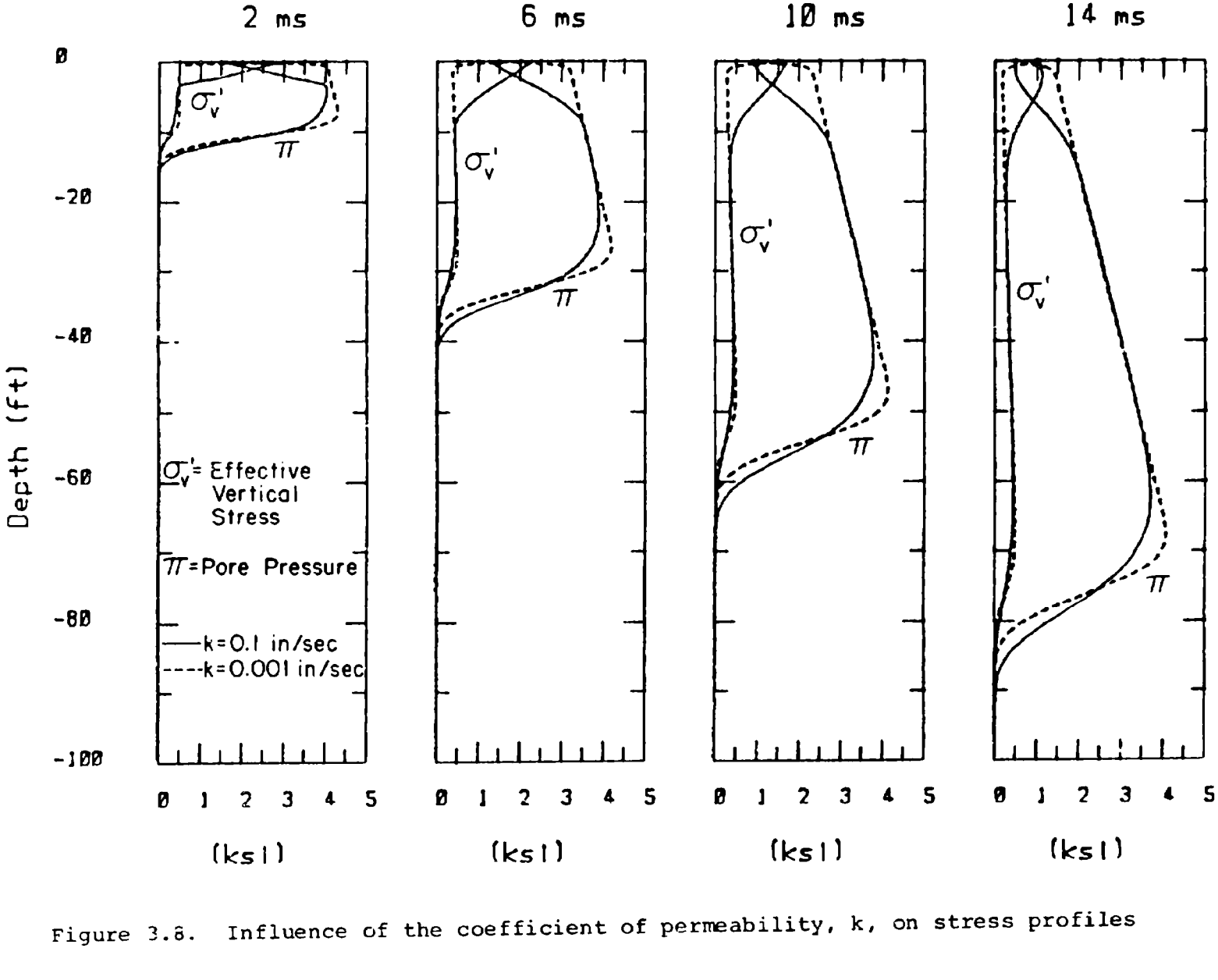

Figure 3.8. Influence of the coefficient of permeability, k, on stress profiles

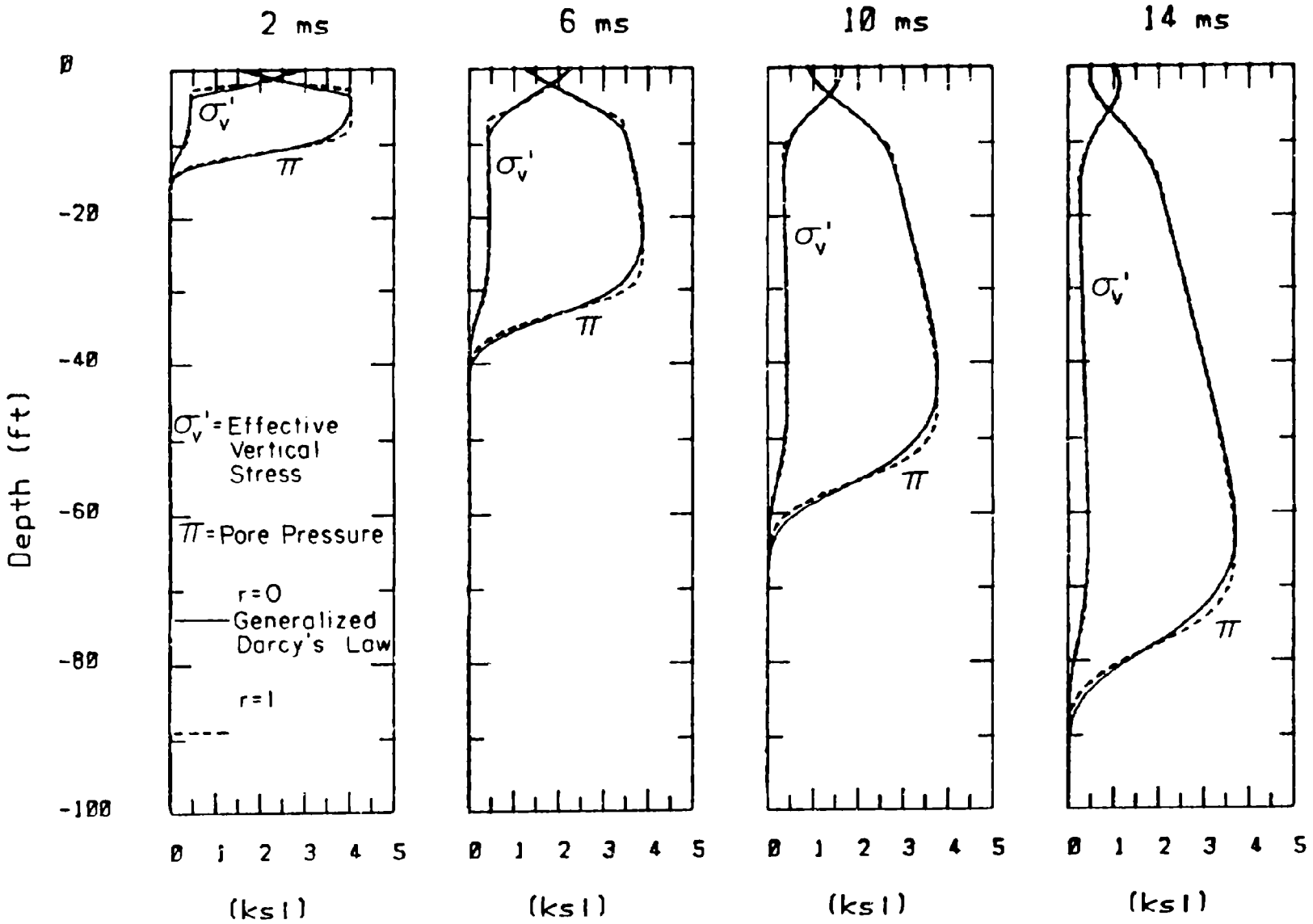

Figure 3.9. Influence of mass increment factor, r, on stress profiles, triangular loading

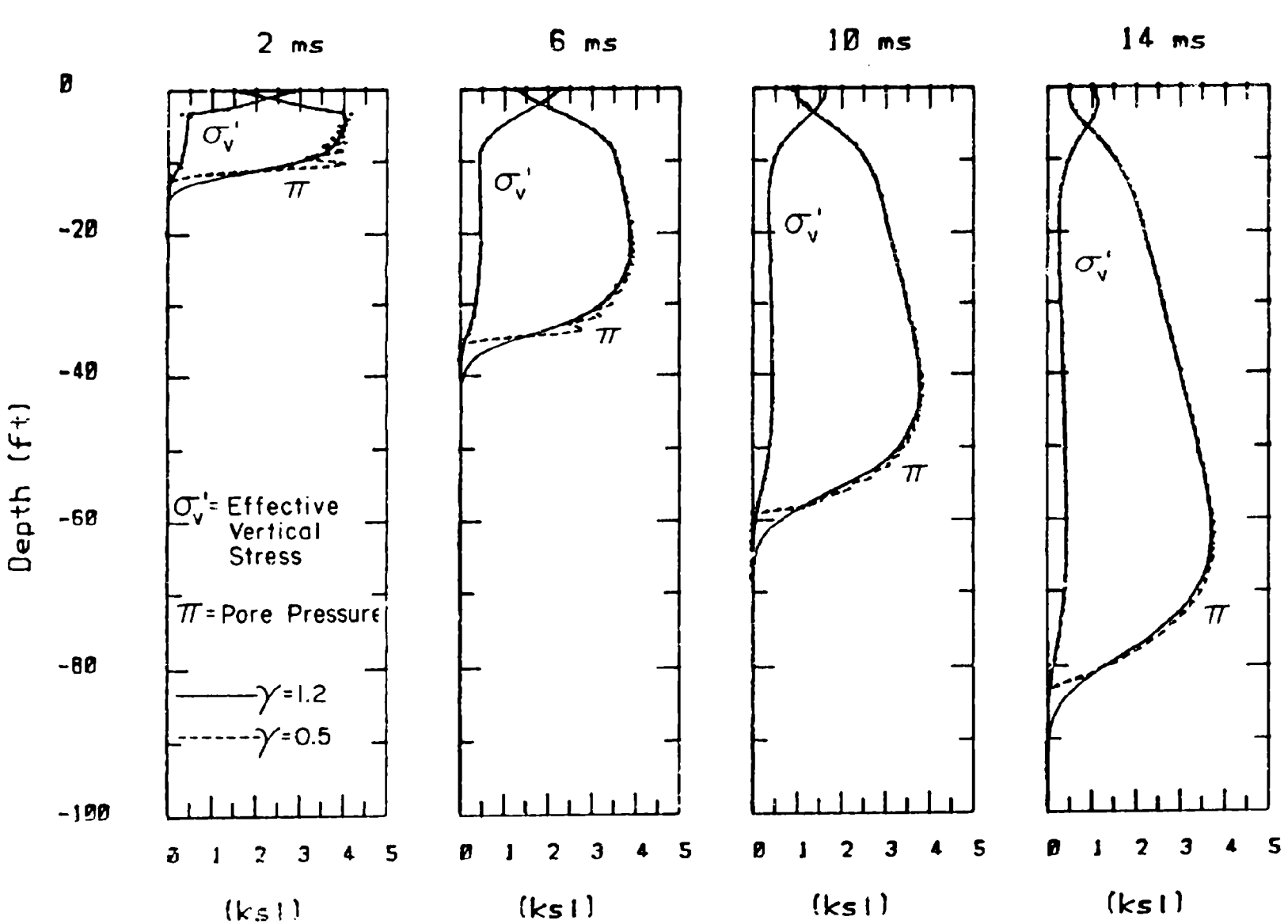

Figure 3.10. Influence of numerical γ damping on stress profiles, γ = 1.2 vs. γ =0.5

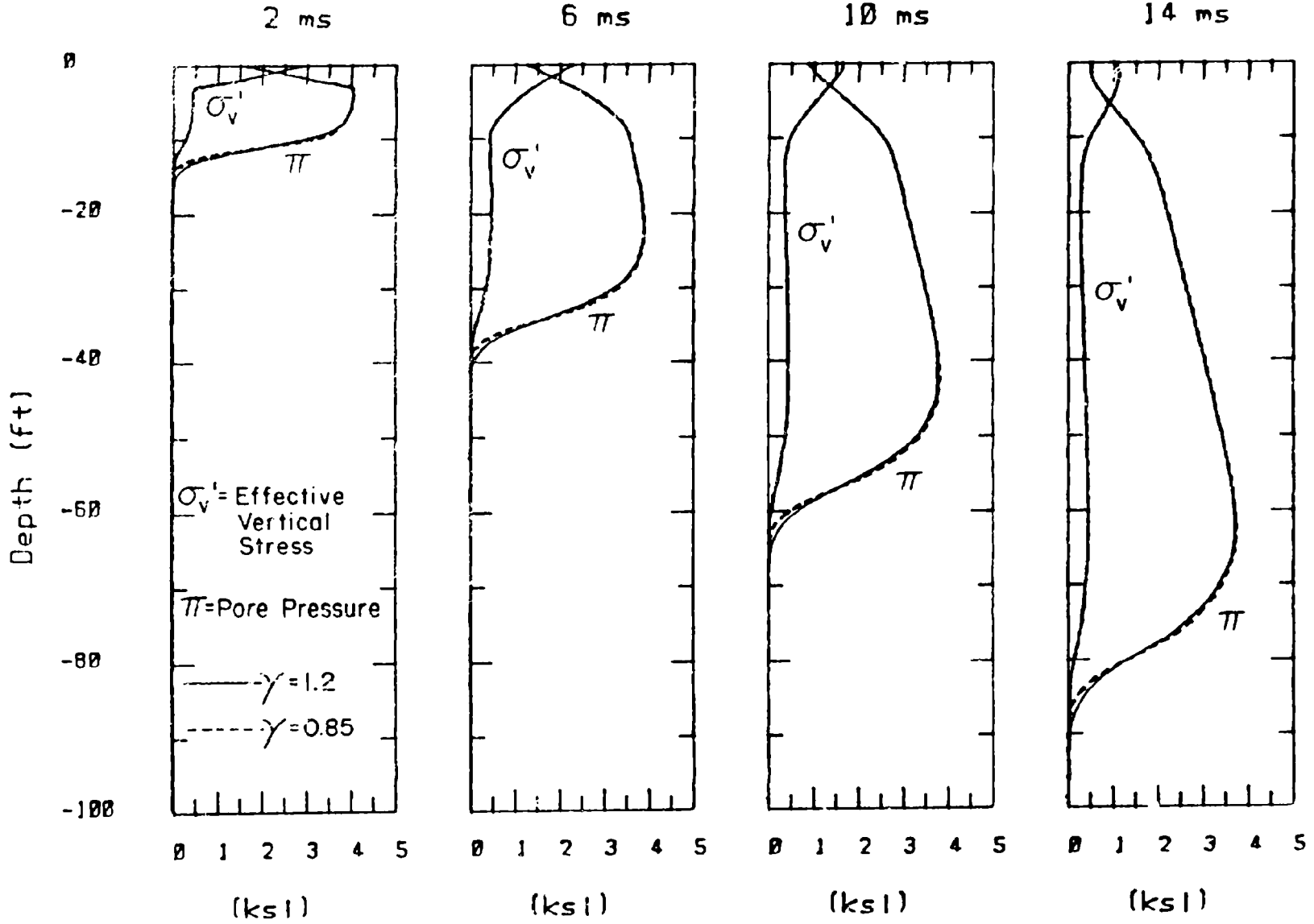

Figure 3.11. Influence of numerical γ damping on stress profiles, γ = 1.2 vs. γ =0.85

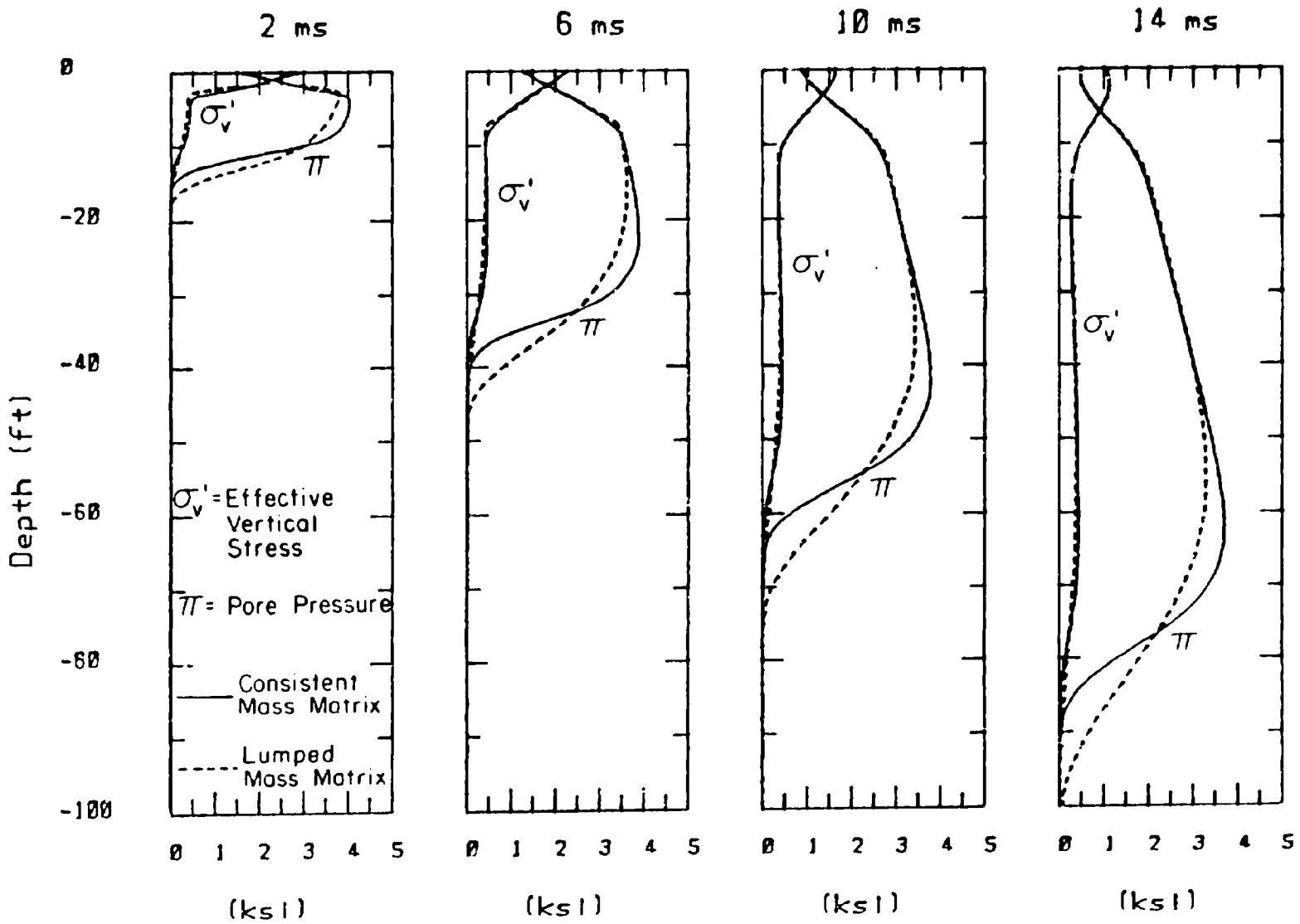

Figure 3.12. Stress profiles from two phase calculations using consistent and lumped mass matrices, triangular loading

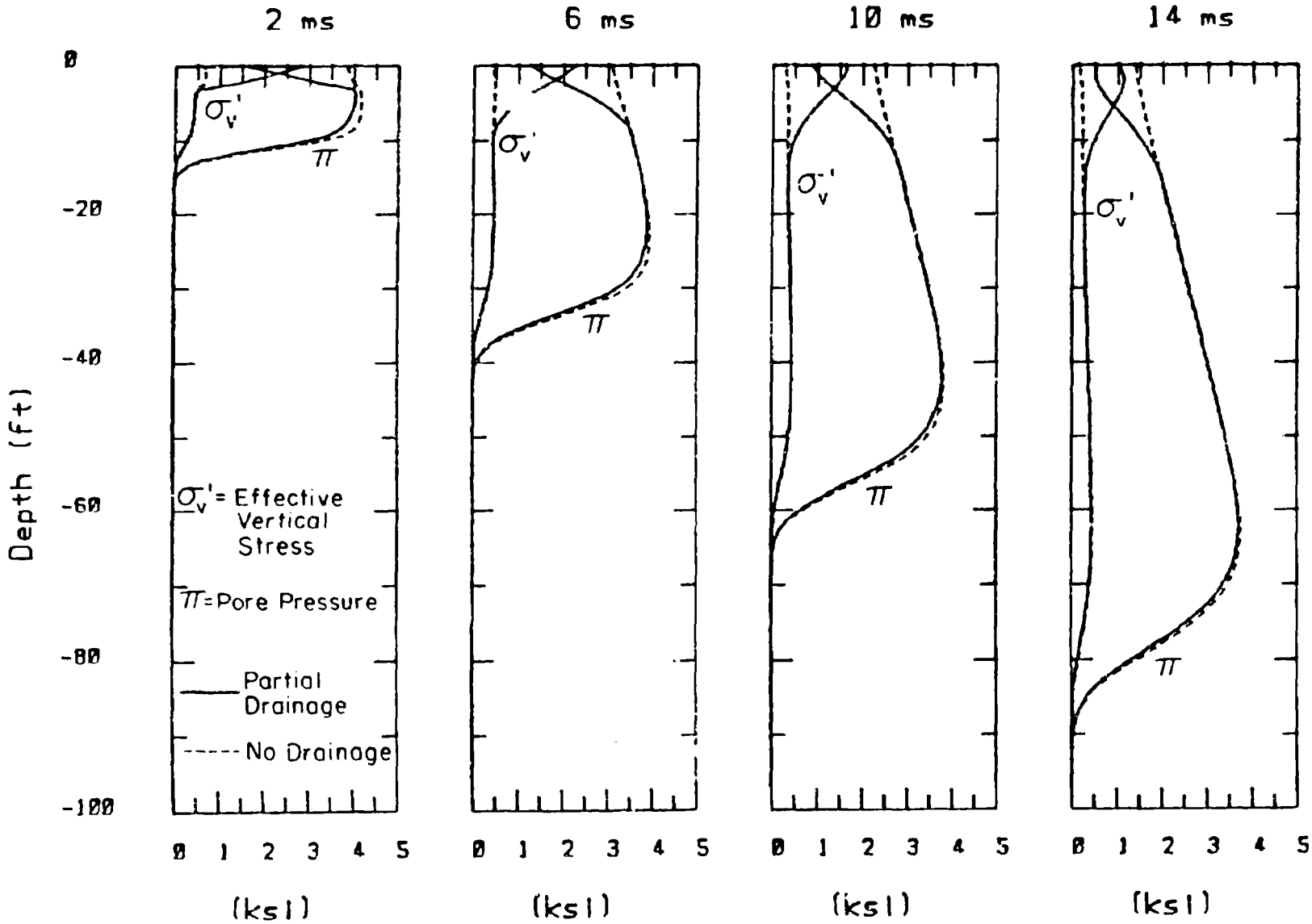

Figure 3.13. Influence of surface drainage conditions on stress profiles, partial drainage vs. no drainage

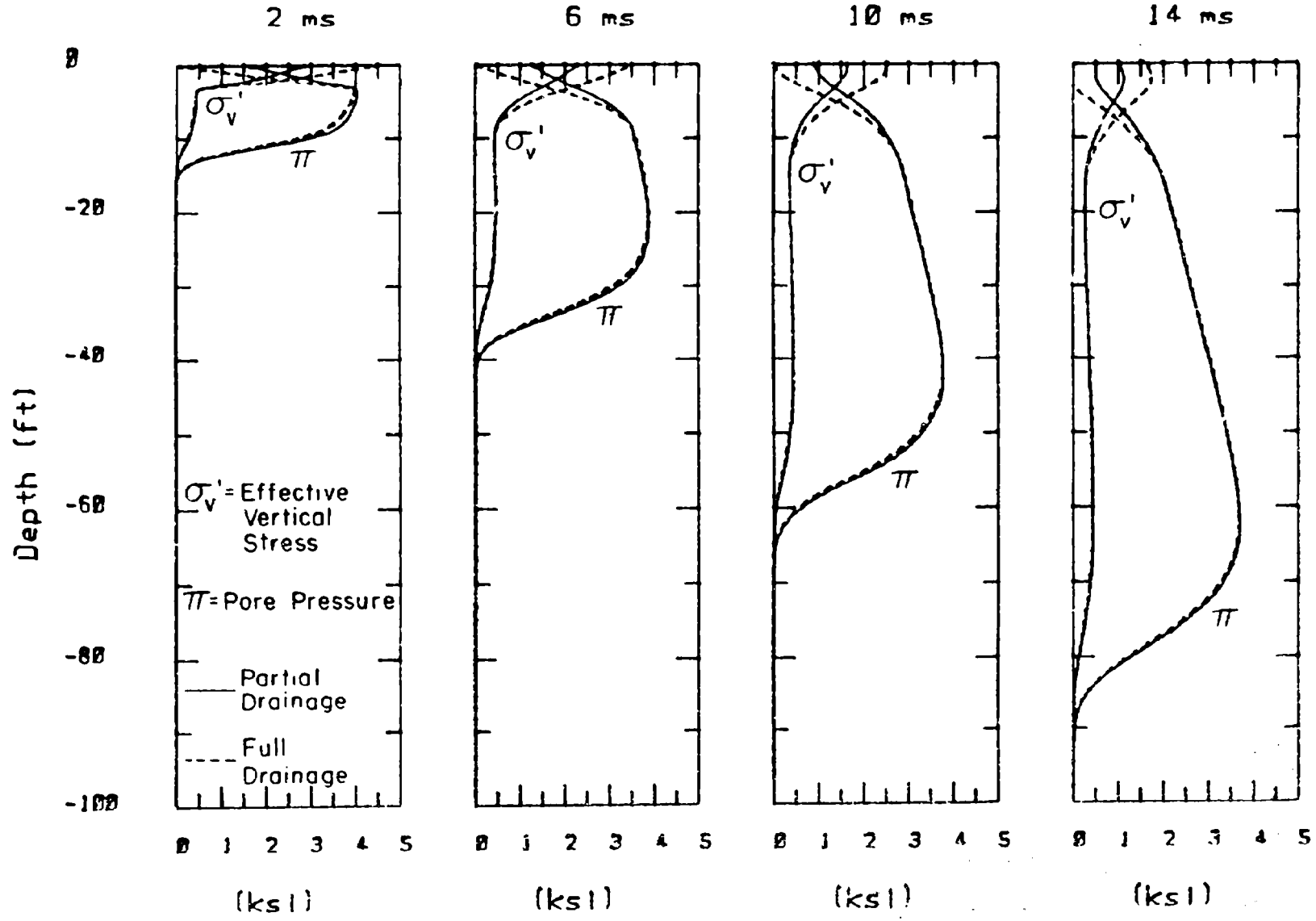

Figure 3.14. Influence of surface drainage conditions on stress profiles, partial drainage vs. full drainage

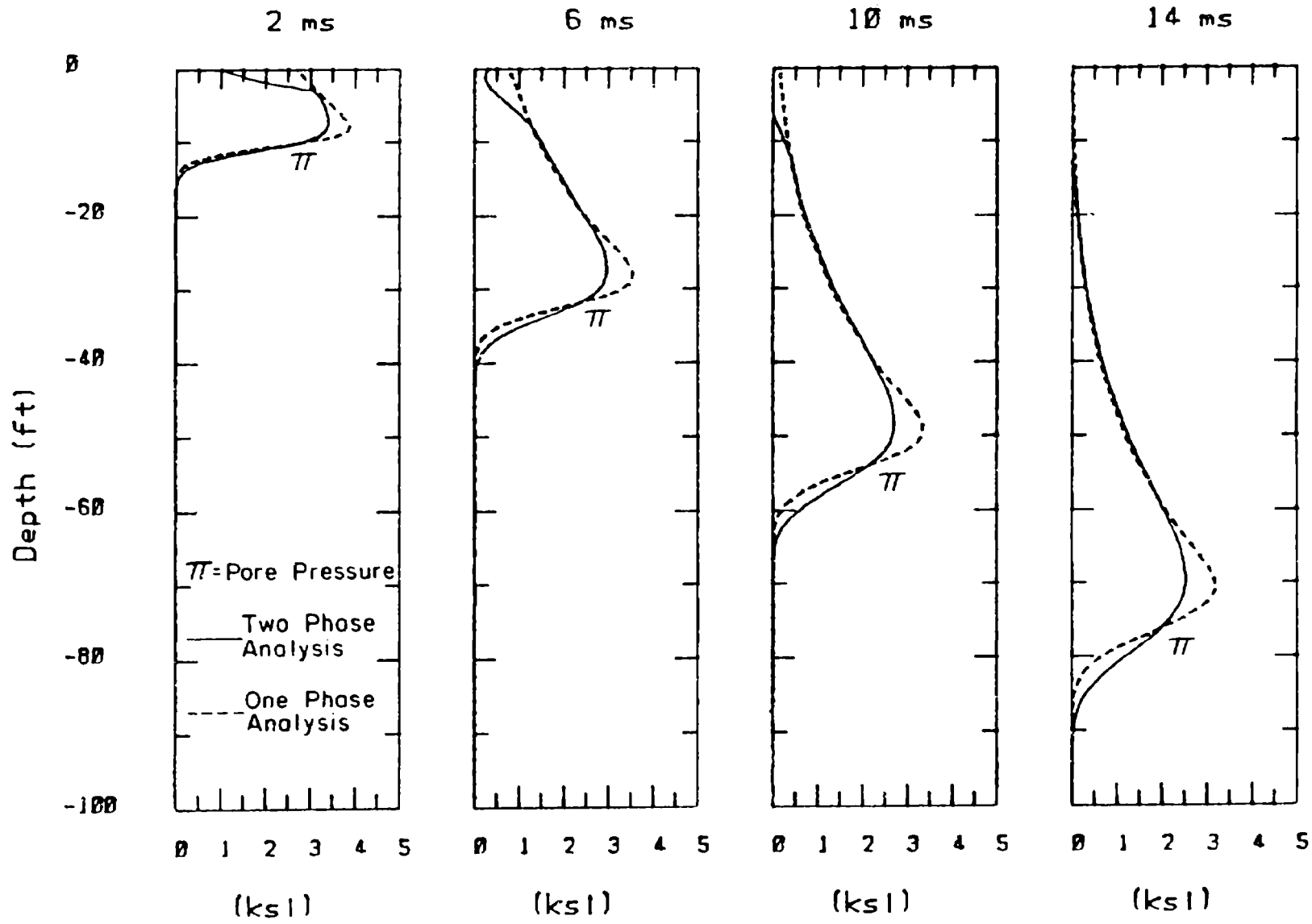

Figure 3.15. Comparison of pore pressure profiles from one and two phase calculations, 5th order polynomial loading

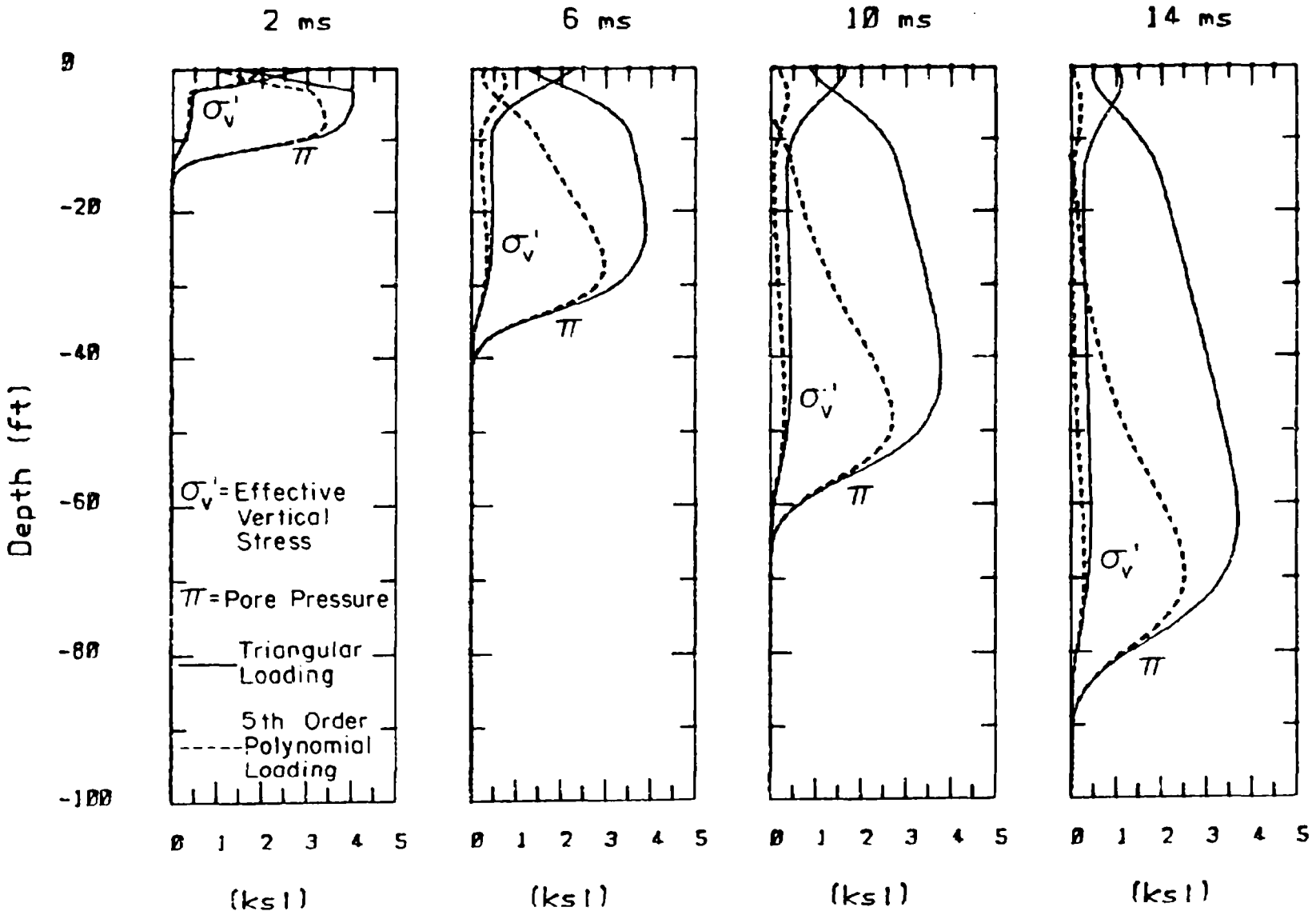

Figure 3.16. Comparison of stress profiles from triangular loading and 5th order polynomial loading

SECTION 4

TWO PHASE DYNAMIC ANALYSIS -

SATURATED POROUS INELASTIC SKELETON

INTRODUCTION

Rischbieter et al., (1977) and other investigators hypothesized that liquefaction could result from one dimensional loadings of saturated soils having hysteretic stress strain response. An analytic formulation of this hypothesis was developed by Blouin and Shinn (1983) which illustrates the liquefaction mechanisms using simple hysteretic material models. The TPDAP code combines these mechanisms with the capability of handling realistic material properties to model wave propagation in continuous two phase media. TPDAP permits the study of liquefaction using realistic loadings and in situ material profiles.

In this section, a brief description of the liquefaction mechanisms discussed above is presented, followed by application of TPDAP in preliminary studies of blast induced liquefaction in two material types. The first is a simple bilinear hysteretic material model, and the second is based on data from uniaxial tests on Enewetak sand presented by Blouin, Martin and McIntosh (1984) and reported as a second volume of this study.

LIQUEFACTION MECHANISMS

The analytic two phase model developed by Blouin and Shinn (1983) treats the stresses and deformations in the soil skeleton as separate entities during compression wave loadings and unloadings. Since granular soil skeletons are hysteretic, expansion of the skeleton during unloading will generally involve only a portion of the volume change which occurred during the compressive wave loadings. During both loading and unloading, however, the pore water behaves elastically. On unloading, the pore water may continue to expand elastically after the skeleton has reached zero effective stress. At this point the expanding pore water will begin to carry the soil particles into suspension and the material will be in a state of liquefaction. Following liquefaction, the soil will consolidate into a more dense state than originally, with the excess pore water pushed upward into overlying unsaturated layers or onto the ground surface. The rate of consolidation will be governed by the amount of excess pore water (i.e. the extent of the zone of liquefaction and the degree of liquefaction) and by the permeability of the liquefied material itself and the permeability of any overlying non-liquefied material.

A crude model depicting both the soil skeleton and the solid/water mixture during uniaxial strain loading and unloading is shown in Figure 4.1. Loading of the soil skeleton occurs along a bilinear path and unloading along a steeper linear path. The initial portion of the loading curve, represented by the loading modulus M_1, is assumed to be elastic and is limited by the maximum strain ε_{ge}, or the corresponding effective stress σ'_{ge}. In instances where the elastic limit is not exceeded, the skeleton will unload along the loading path and there will be no inelastic volume decrease in the soil skeleton. The elastic portion of the loading curve can represent either a cemented soil or simply a short elastic portion of the loading curve commonly evidenced

during field tests known as the seismic or elastic toe. Beyond the elastic strain limit ε_{ge}, the skeleton is no longer elastic and loads at a modulus M_2, and unloads at a much stiffer modulus M_u.

According to Terzaghi's effective stress law, the total stress, σ, applied to an increment of saturated soil will be carried by the pore water pressure, π, and by the intergranular stress, σ'_g, within the soil skeleton. The pore water pressures may exceed the intergranular stresses by an order of magnitude. In order for liquefaction to occur upon unloading, two conditions must be met. The first is simply that the elastic strain limit in the soil skeleton must be exceeded during loading to the peak dynamically applied stress σ_p. Otherwise, both the soil skeleton and pore water will unload elastically and no excess pore pressures will be generated. Figure 4.1 depicts deformation in the skeleton and soil-water mixture at depth d where the initial effective overburden stress is σ'_{gd} and the initial pore pressure is π_d. Note that the in situ strain in each case is taken as zero and that stresses are measured from the in situ conditions. The first condition for liquefaction is satisfied when the strain in the soil skeleton exceeds the elastic limit ε_{ge}. If no relative flow between the pore water and skeleton is assumed, then the strain in the solid/pore water mixture equals that in the skeleton. Upon unloading, the stiff skeleton unloading modulus results in a rapid drop in effective stress until it reaches zero at the strain ε_{go}. At this point, the skeleton has lost all strength and reaches the liquefied state. Unloading continues until the stress in the soil-water mixture reaches the effective overburden stress σ'_{gd} at the strain ε_{mr}. Between strains ε_{go} and ε_{mr}, the expanding pore water tends to carry the soil particles into suspension. Finally, as the particles reconsolidate, the pore pressure gradually drops from σ'_{gd} back to its original value π_d.

BILINEAR MODEL

The triangular loading pulse from Figure 3.1 was applied to a saturated material having bilinear load-unload characteristics. All properties of the skeleton are the same as those used in the previous section, given in Table 3.1, except the unloading moduli are taken as three times the corresponding loading moduli. Thus, hysteresis is introduced into the material skeleton with a strain recovery ratio of 1/3.

The results of this calculation are plotted as a solid line in Figure 4.2. The effective stress and pore pressure profiles at four times, from 2 to 14 msec, are compared to those from the corresponding calculations using the linear elastic model. At 2 msec there is no apparent difference between the calculations. At later times, however, the different unloading slopes affect the response behind the stress peaks. This effect becomes more pronounced with increasing depth and time. As explained in the previous subsection, during unloading the bilinear skeleton will tend to recover only 1/3 of the loading strain, and the skeleton stress will drop proportionately faster. For a totally undrained loading using this set of bilinear properties, the effective stress would be expected to drop to zero about 1/3 of the way into the unloading. At 14 msec the effective stress in Figure 4.2 drops to zero at a depth of about 22 ft, at approximately 1/3 of the way into the unloading. At this point, the soil particles would tend to begin separating and a state of liquefaction would exist. In this bilinear calculation, however, tension is allowed to develop in the soil skeleton, so the post-liquefaction process is not accurately depicted.

Because of the hysteresis in the bilinear skeleton, the effective stress drops faster during unloading than the effective stress in the elastic case. The pore pressure behind the wavefront in the bilinear material drops less rapidly than the pore pressures in the linear material, compensating for the more rapid effective stress drop in the bilinear soil. The total stresses are about equal in both calculations.

The inelastic behavior of the skeleton also causes additional energy attenuation due to the hysteretic material damping. Careful examination of the 14 msec profile in Figure 4.2 shows that the total stress behind the wavefront is lower in the bilinear material than that in the elastic case. This difference evidently results from the hysteretic damping.

Figure 4.3 is an expanded view of the bilinear effective stress and pore pressure profiles at 15, 16 and 17 msec. A zone of effective tensile stress is developing at these later times. This zone extends from a depth of about 14 ft to a depth of 40 ft at a time of 17 msec. This developing tensile zone is indicative of liquefaction, but because tensile stresses are allowed to develop in the skeleton and because there are no gravitational stresses in this calculation, it does not realistically model the liquefaction process.

ENEWETAK SAND

The final set of parametric calculations undertaken in this study examines the response of saturated sand from Enewetak Atoll. The skeleton properties are taken from laboratory data reported in the second volume of this study by Blouin, Martin and McIntosh (1984). The sand is a uniform carbonate beach sand with a mean grain diameter of about 0.5 mm and a porosity of 45%.

Properties selected for this sand are shown in Figure 4.4. The loading modulus is a stepwise approximation to the actual constrained compression data from test 12. The unloading modulus is expressed as a function of peak stress according to

$$M_u = 3470\ \sigma'^{(0.651)}_{am} \qquad (4\text{-}1)$$

where σ'_{am} is the maximum previous axial stress expressed in psi. As indicated by the data, the unload modulus becomes continually stiffer with increasing peak stress.

Three uniaxial strain calculations were performed on the saturated Enewetak sand. All used a triangular loading with duration and risetime as specified in Figure 3.1. The peak stress in the first two calculations was 50 ksi and the peak stress in the last calculation was 5 ksi. Unlike the bilinear calculations, tensile stress was not allowed to develop in the Enewetak sand. Whenever the effective stress dropped to zero, the skeleton had no strength and the modulus dropped to zero.

50 ksi Peak Stress

The two 50 ksi calculations examined the influence of the surface drainage conditions. Neither calculation included in situ stresses due to gravity. In addition to the usual effective stress and pore pressure profiles, motion and stress time histories at selected depths are also presented. Figure 4.5 shows the stress profiles from the two calculations at 2, 6, 10 and 14 msec. Because the skeleton modulus of the Enewetak sand was considerably lower than that of the previous skeletons analyzed in this study, the effective stress profiles are expanded by a factor of ten in Figure 4.5 to afford better definition. The most significant feature of both sets of

effective stress profiles is the development of a large zone of liquefaction behind the wavefront. By 14 msec this zone extends from the surface to a depth of 42 ft.

There is little difference between the profiles for the two different surface drainage conditions. The partial surface drainage condition was attained by partitioning the airblast loading between the pore water and soil skeleton in proportion to the porosity. Thus, 45% of the total load was applied to the pore water and the remaining portion to the soil skeleton. In the calculation with no surface drainage, relative motion between the soil skeleton and pore water was prohibited at the loading boundary. As was also observed in the linear elastic analysis, the surface stress distribution is rapidly repartitioned so that the undrained surface loading profile is approximated within a very short distance beneath the surface. In other words, the surface load partitioning/drainage conditions affect only the very near surface response. The overall response is insensitive to the assumed surface drainage conditions.

Time histories of the response of the soil skeleton at a depth of 10 ft are shown for both the partial surface drainage and no surface drainage calculations in Figure 4.6. The top time history compares the effective vertical and horizontal stresses from the two calculations, and the remaining time histories compare the displacement, velocities and accelerations. As mentioned in the above discussion of the stress profiles, the influence of surface drainage is small. According to the effective stress time histories, liquefaction occurs at the 10 ft depth shortly after 6 msec. The peak vertical effective stress in the skeleton is approximately 1400 psi and the peak horizontal effective stress, controlled by the K_o value of 0.5, is about 700 psi. Thus, the peak skeleton stress at this depth is only 2.8% of the 50 ksi peak loading stress. Since so little stress is carried in the skeleton, the influence of the liquefaction on the overall skeleton motions during the constrained dynamic loading

is negligible. However, it should be noted that the material in the liquefied condition no longer has any shear strength. This can result in very large mass movements at late times under gravitational or other loadings whenever nonuniform stress fields exist.

The corresponding pore pressure time histories and apparent relative fluid motions between the pore water and soil skeleton at the 10 ft depth are plotted in Figure 4.7. As described in the theoretical discussion of Section 2, the apparent relative fluid motion equals n times the actual relative motion where n is the porosity. In the Enewetak sand, the actual relative motions between the particles and pore water is 2.2 times the apparent values. The pore pressure time histories resemble the triangular loading pulse. Peak pressures are about 43 ksi, over 30 times higher than the peak vertical stress in the soil skeleton at this depth. The displacement time history indicates that the pore water moves downward relative to the soil skeleton during the dynamic loading. The peak magnitude of apparent relative displacement is approximately 0.9 in and occurs just after 6 msec, which also is the time at which liquefaction occurs.

The velocity time histories indicate a sharp downward velocity relative to the soil skeleton at the wavefront. The peak apparent relative downward velocity is about 47 ft/sec and the actual peak relative velocity is about 103 ft/sec. This occurs at 2.4 msec. It compares to a peak downward velocity in the soil skeleton of approximately 325 ft/sec, though this peak is reached somewhat later at about 4 msec. The apparent relative velocity decays rapidly from its peak value and levels off at about 4 ft/sec by 5 msec. Just after 6 msec, at the time of liquefaction, the velocity suddenly reverses direction and becomes stable in the upward direction with a magnitude of 5 ft/sec. This reversal is evidently associated with the

liquefaction. The reversal in velocity controls the time of peak in the apparent relative displacement time history.

The apparent relative acceleration is initially downward with a peak value of about 2700 gs. This compares to a peak skeleton acceleration of 14000 gs. The apparent relative acceleration quickly reverses at 2.4 msec and reaches a peak deceleration of about 900 gs at 2.8 msec. It then tapers off to near zero slightly after 5 msec and registers a small negative value at the time of liquefaction.

Figures 4.8 and 4.9 present stress and motion time histories for the 50 ksi triangular loading at a depth of 20 ft for the undrained surface loading condition. These waveforms are similar to those at the 10 ft depth of Figures 4.6 and 4.7. As shown in the effective stress time histories of Figure 4.8, liquefaction occurs at 8.4 msec at the 20 ft depth. The peak apparent relative velocity between the pore water and the skeleton is 41 ft/sec at this depth and the peak apparent relative acceleration is about 1700 gs. As was the case at the 10 ft depth, the relative velocity reverses at the time of liquefaction indicating that the pore water begins to move upward relative to the soil skeleton.

5 ksi Peak Stress

The effective stress and pore pressure profiles as functions of time and depth for the final Enewetak sand calculation are presented in Figure 4.10. The applied loading was the 5 ksi triangular pulse from Figure 3.1 with no surface drainage permitted at the loading boundary. In this calculation gravitational stresses were included on both the soil skeleton and the pore water. The initial in situ effective stress is apparent in all the profiles, where the effective stress increases linearly with depth and at 100 ft equals 43 psi.

Coincidentally, the pore pressure under the gravitational loading also is 43 psi at that depth. Because the effective stress profiles are magnified by a factor of 10 compared to the pore water pressures, the 43 psi pore pressure is barely noticeable in the scale of Figure 4.10.

Several differences are apparent between the 5 ksi loading profiles of Figure 4.10 and the 50 ksi loading profiles of Figure 4.5. At 10 msec the peak effective stress in the 5 ksi case is only about 1.6% of the peak pore pressure. In the 50 ksi loading at this time, the peak effective stress is about 3.6% of the peak pore pressure. The significantly greater portion of the total stress carried in the pore skeleton under the 50 ksi loading is due to the increase in skeleton modulus with increasing strain indicated in the skeleton properties of Figure 4.4. Under the 50 ksi loading the skeleton strains are proportionally higher than those under the 5 ksi loading; thus, the increasingly stiff skeleton modulus at these higher strains results in a relatively greater portion of the total stress distributed to the skeleton.

Another difference observed in Figure 4.10 is the increase in dynamic peak effective stress with increasing time and depth. This is in contrast to the decreasing peak effective stress in the 50 ksi loading. Here the difference is due to the application of the gravitational effective stress in the 5 ksi case. With increasing depth, the initial in situ effective stress increases and the skeleton, in essence, becomes stiffer with increasing depth. Thus, for a given peak total stress level, the portion of the total stress carried in the skeleton would be less at shallow depths than it would be at deeper depths. However, because peak stress attenuates with increasing depth due to hysteretic and fluid damping, the net change in peak effective stress depends on the summation of these two effects. In this case, the net result is an increase in effective stress with increasing depth.

In the 5 ksi loading calculations with gravitational stresses, the soil also liquefied during unloading from the peak dynamic stress. As shown in Figure 4.10, at 14 msec the soil is liquefied from the surface to a depth of about 36 ft. This is somewhat less than the 42 ft depth of liquefaction shown in Figure 4.5 for the 50 ksi load at 14 msec.

Effective stress and skeleton motion time histories at the 10 ft and 20 ft depths for the 5 ksi loading are shown in Figure 4.11 and 4.13 respectively. The pore pressure and apparent relative motion time histories for the 10 ft and 20 ft depths are shown in Figures 4.12 and 4.14. The waveforms in these examples are similar to those presented in the corresponding Figures 4.6 through 4.9 for the 50 ksi loading. The magnitudes are correspondingly lower for the 5 ksi loading. The only significant difference appears to be that the apparent relative velocity of the pore water becomes negative relative to the skeleton prior to liquefaction in the 5 ksi case. Thus, velocity reverses gradually during the initial unloading rather than abruptly at the time of liquefaction.

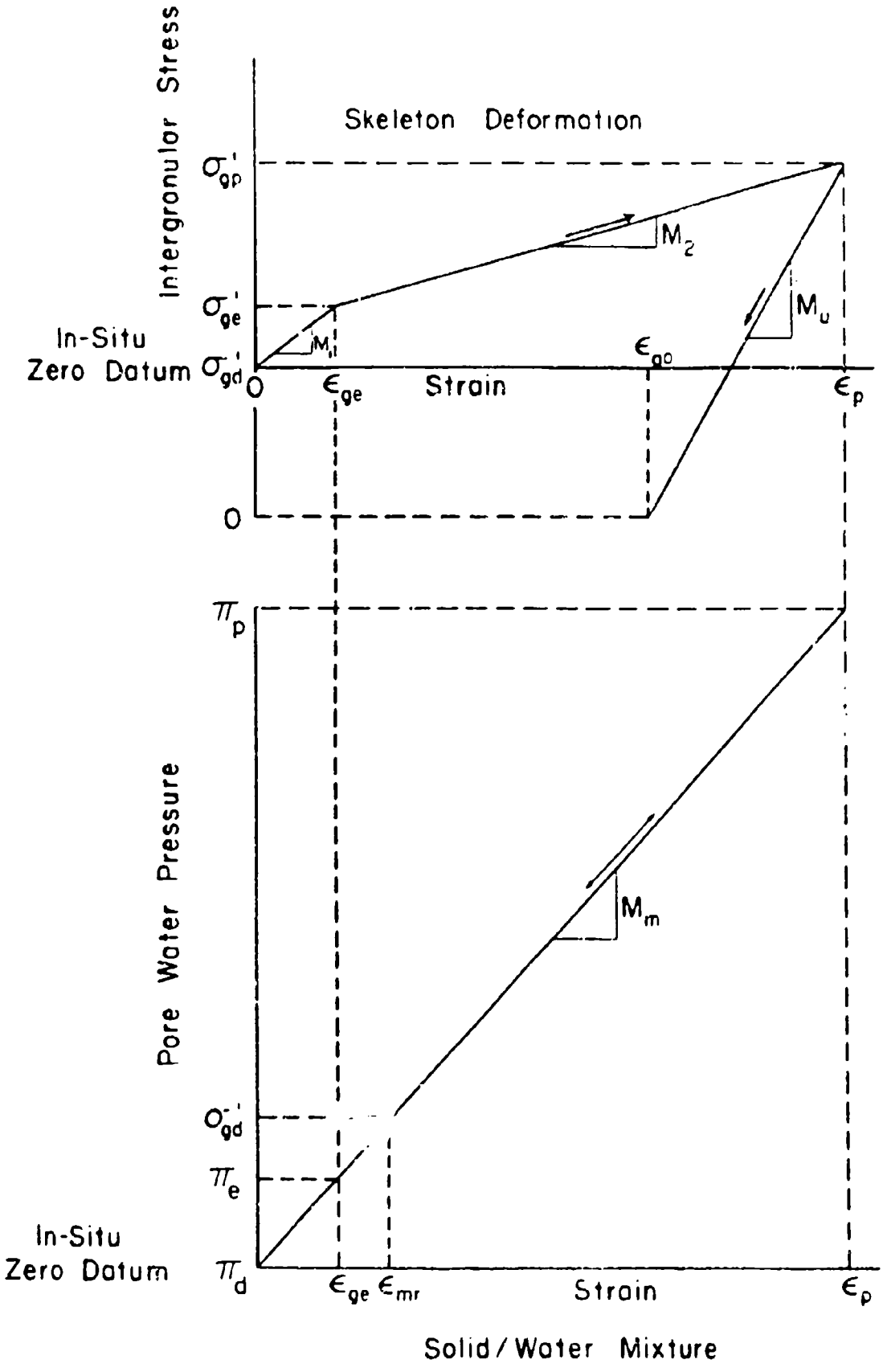

Figure 4.1. Schematic representation of deformation in saturated granular soil

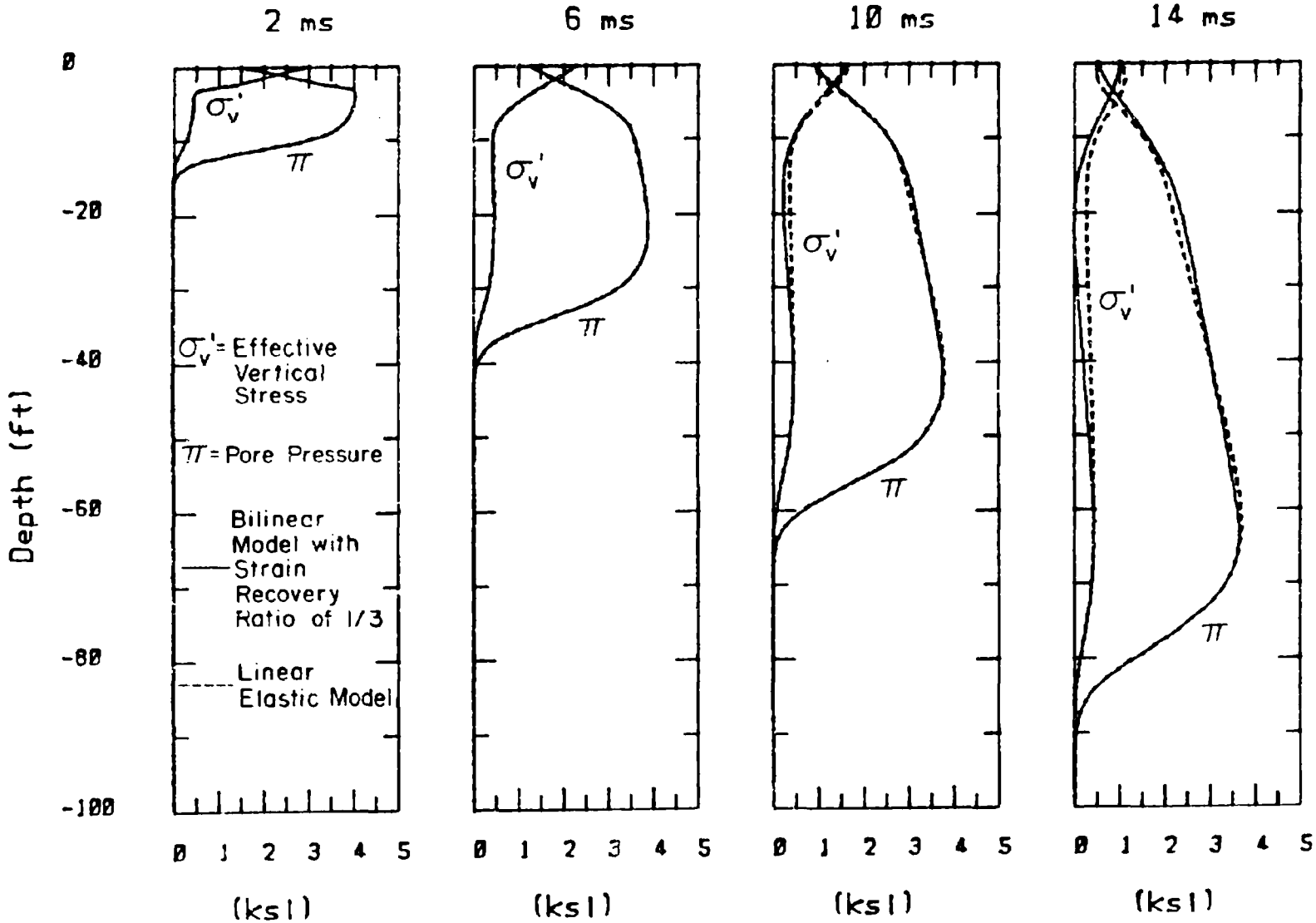

Figur ' 2. Stress profiles in bilinear material, compared with linear elastic material

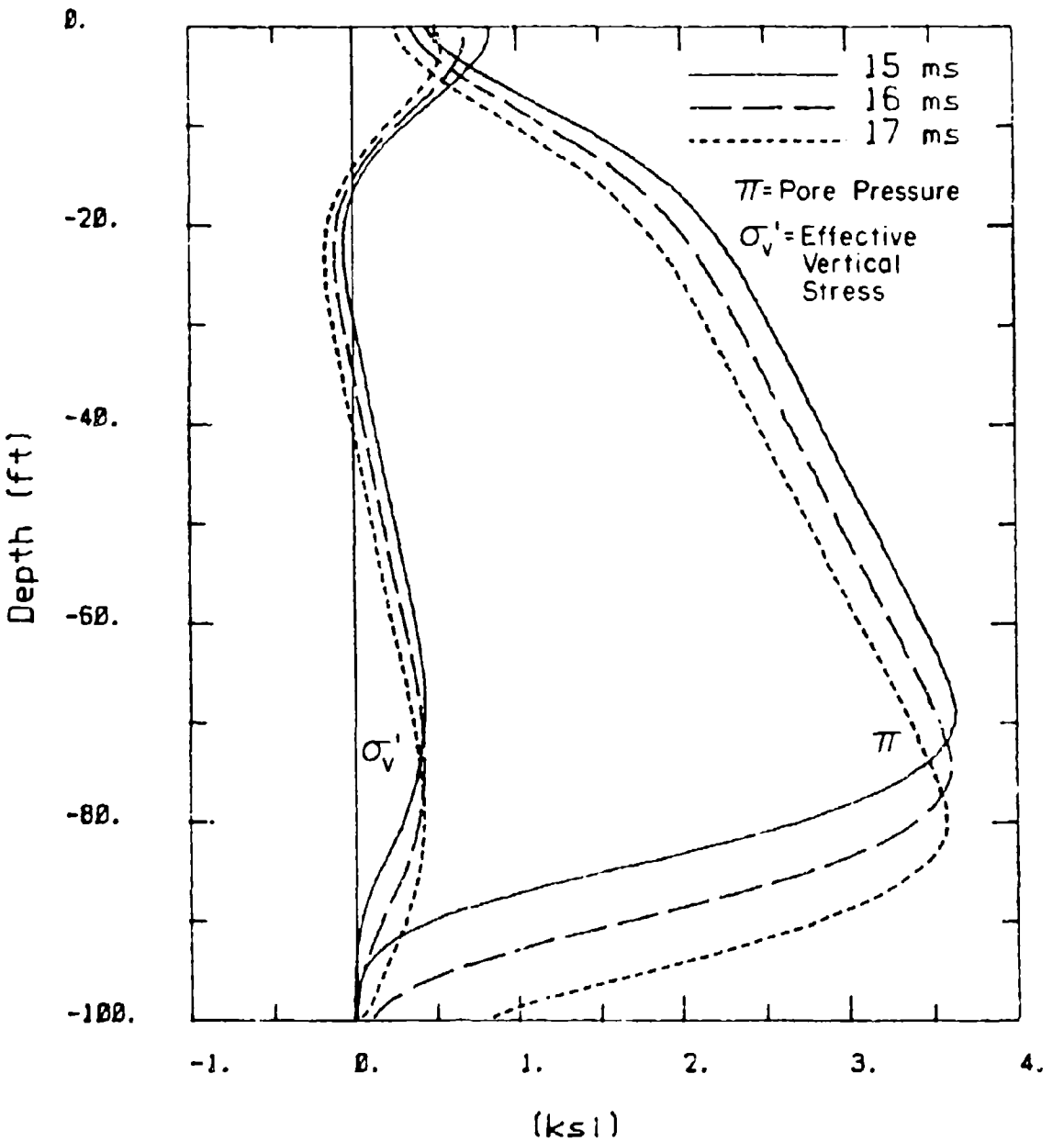

Figure 4.3. Stress profiles in bilinear material at 15, 16 and 17 msec

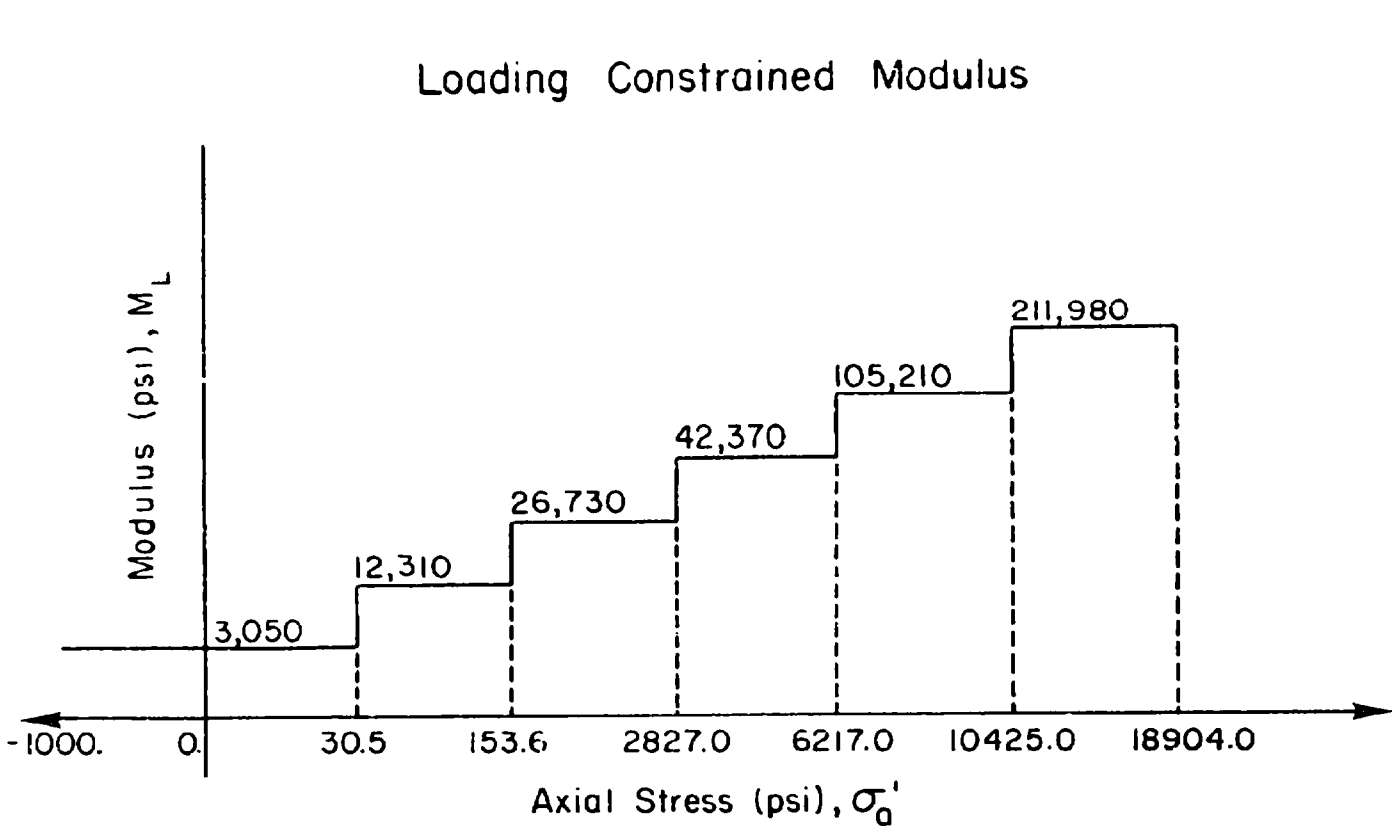

Unloading Constrained Modulus

$$M_u = 3470\ \sigma'^{0.651}_{am} \quad \text{(psi)}$$

σ'_{am} = maximum previous axial stress (psi)

$K_o = 0.5$ for loading and unloading

Figure 4.4. Loading and unloading skeleton constrained moduli of Enewetak sand

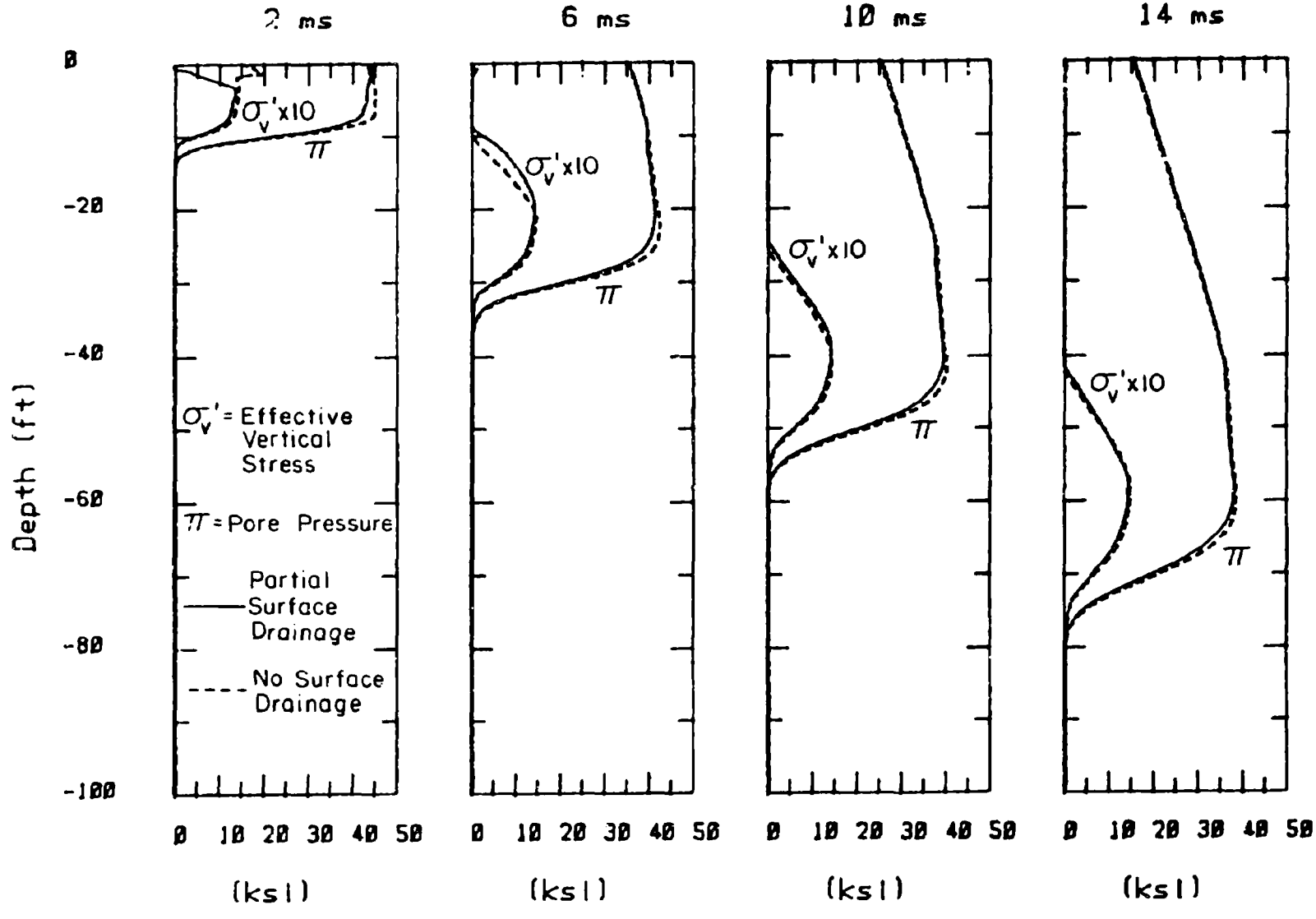

Figure 4.5. Influence of surface drainage on stress profiles, 50 ksi triangular loading of Enewetak sand

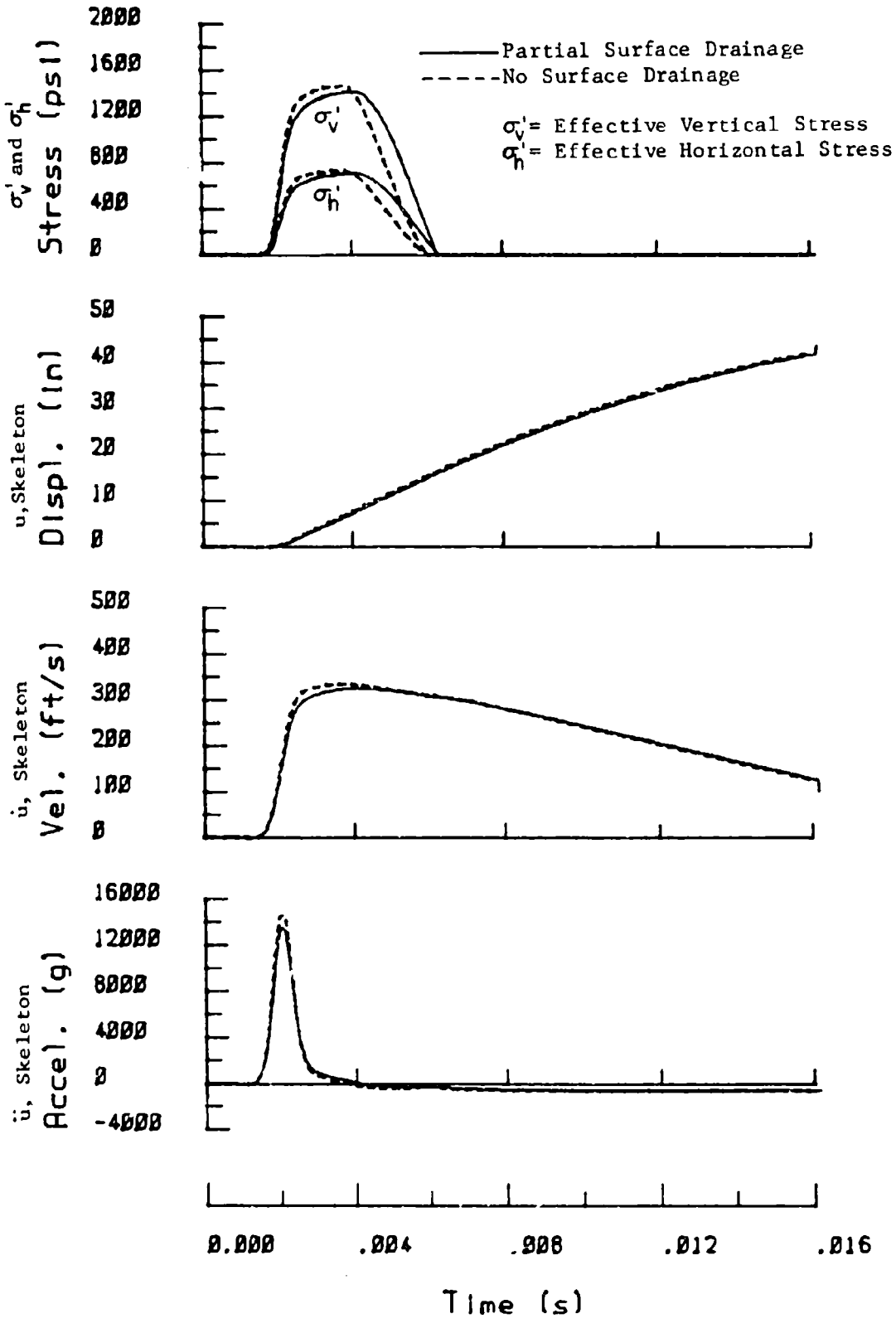

Figure 4.6. Effective stress and skeleton motion time histories at 10 ft depth, 50 ksi triangular loading

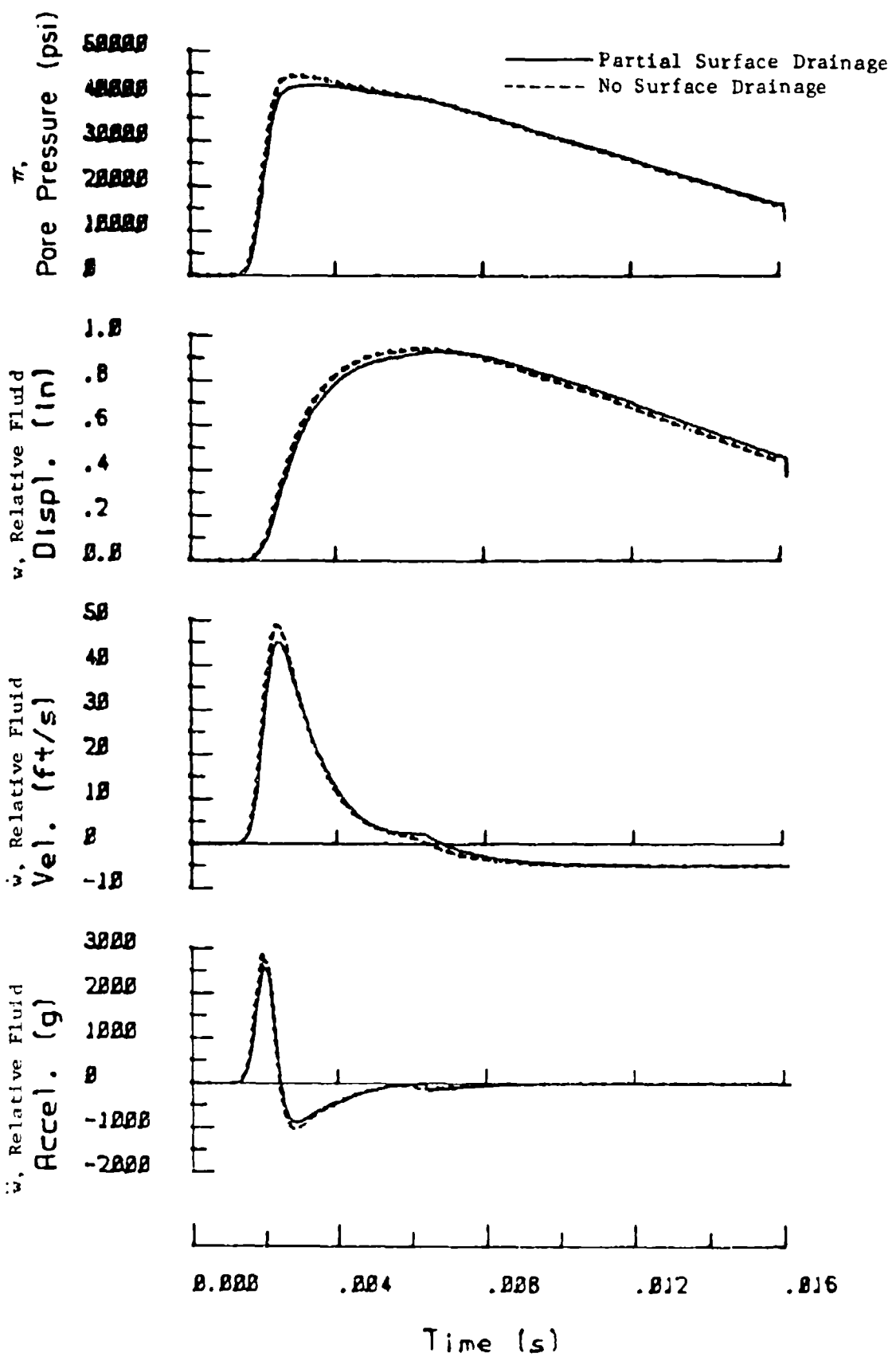

Figure 4.7. Pore pressure and apparent relative fluid motion time histories at 10 ft depth, 50 ksi triangular loading

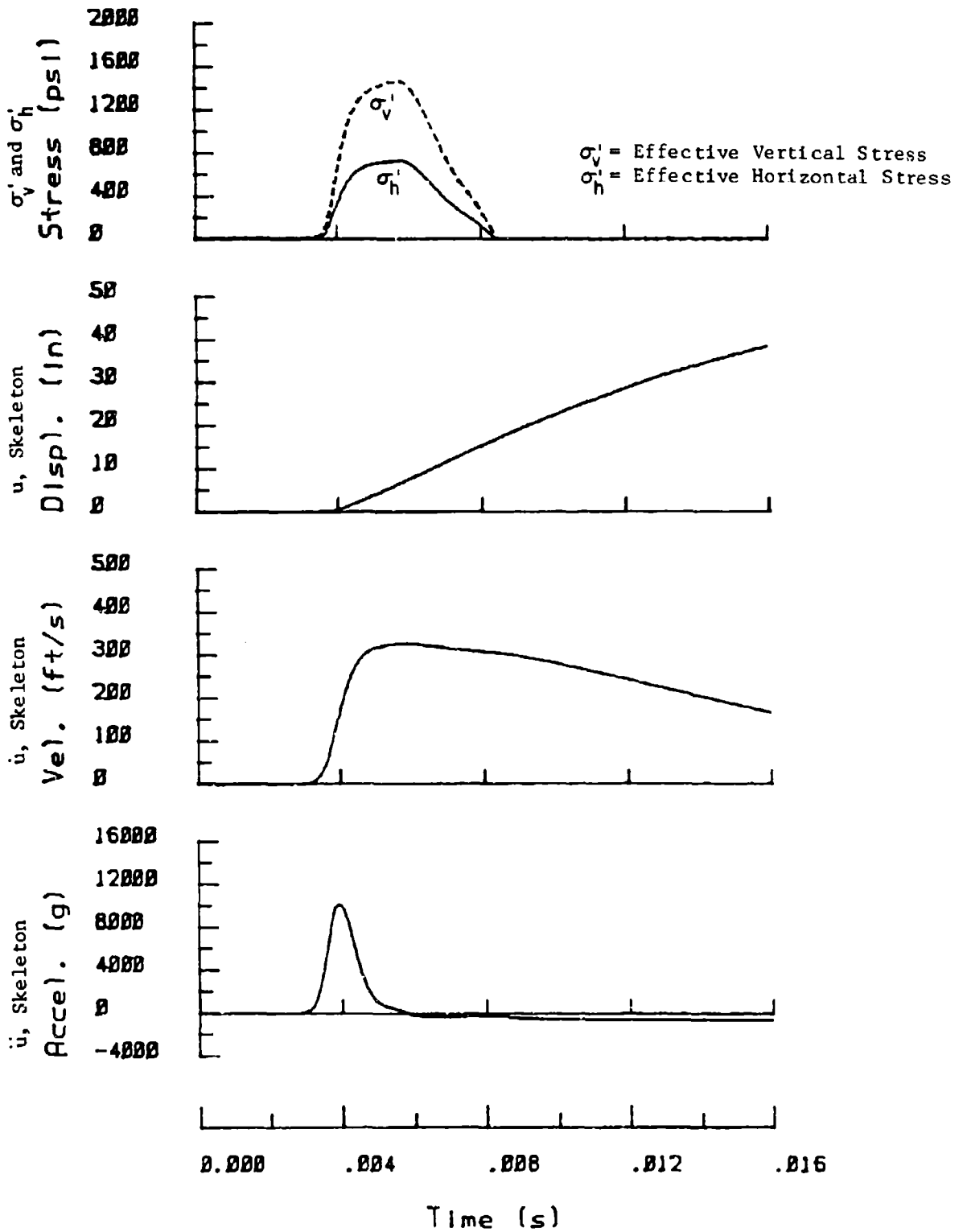

Figure 4.8. Effective stress and skeleton motion time histories at 20 ft depth under 50 ksi triangular loading, no surface drainage

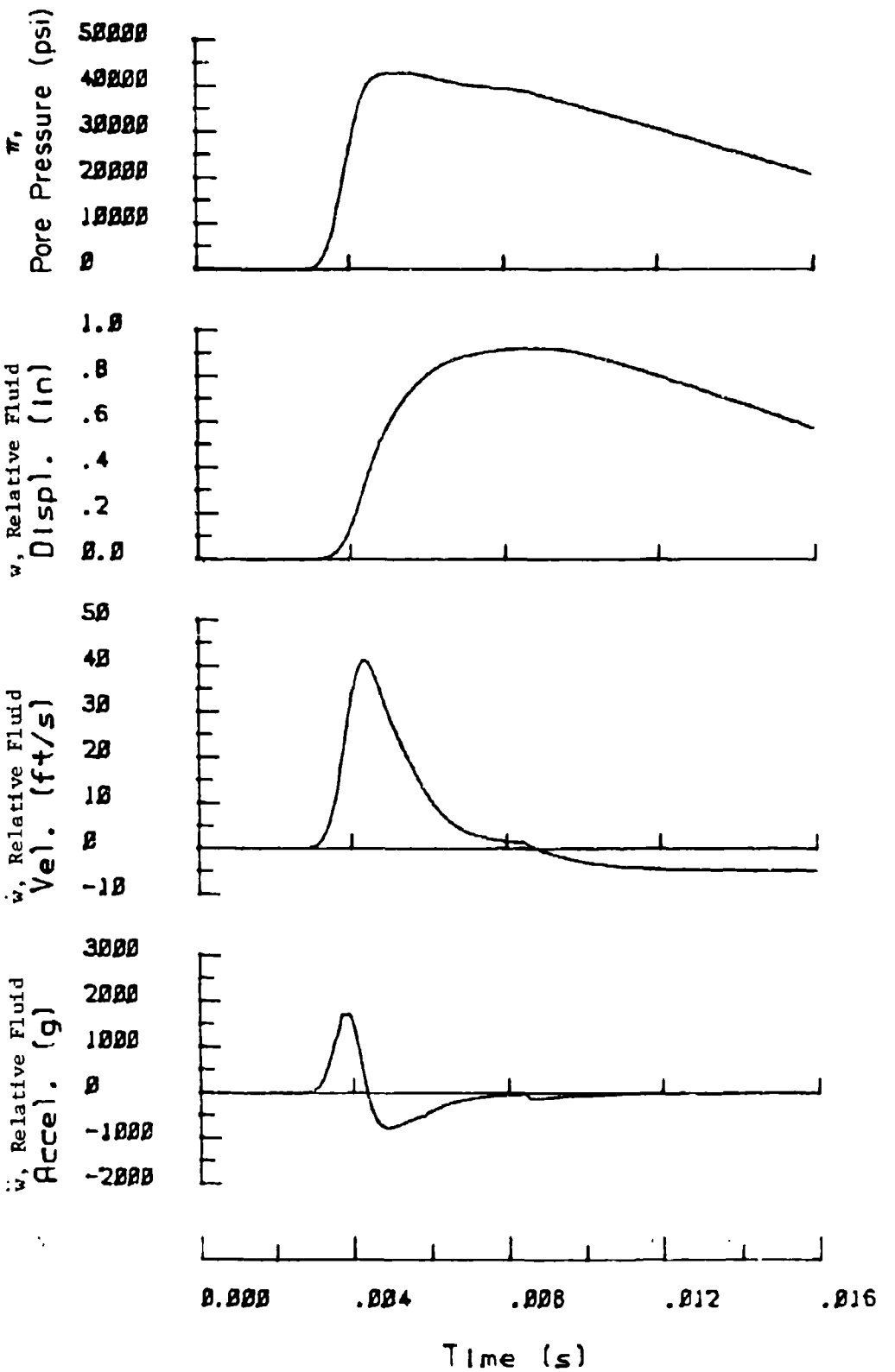

Figure 4.9. Pore pressure and apparent relative fluid motion time histories at 20 ft depth under 50 ksi triangular loading, no surface drainage

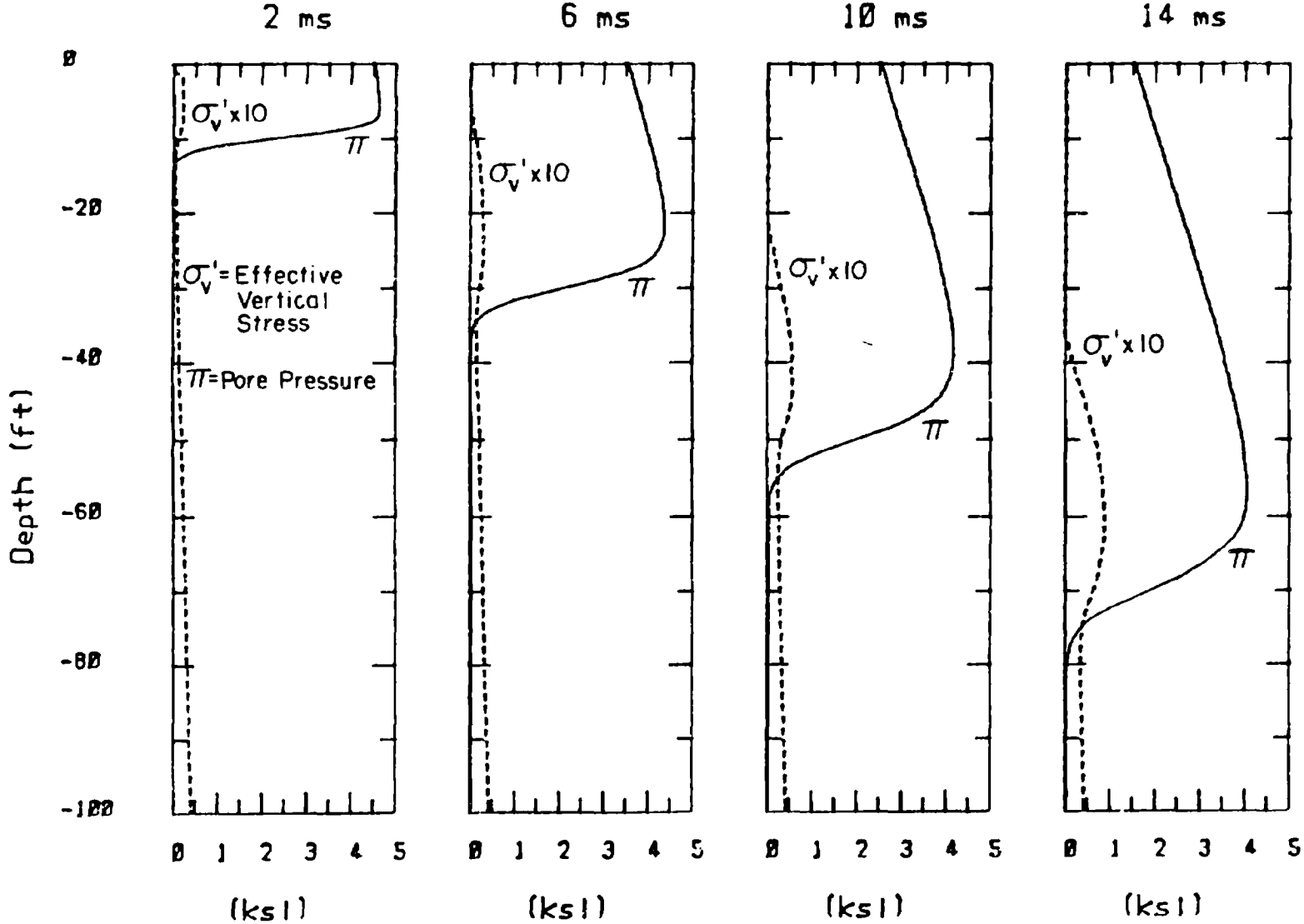

Figure 4.10. Stress profiles under 5 ksi triangular loading of Enewetak sand

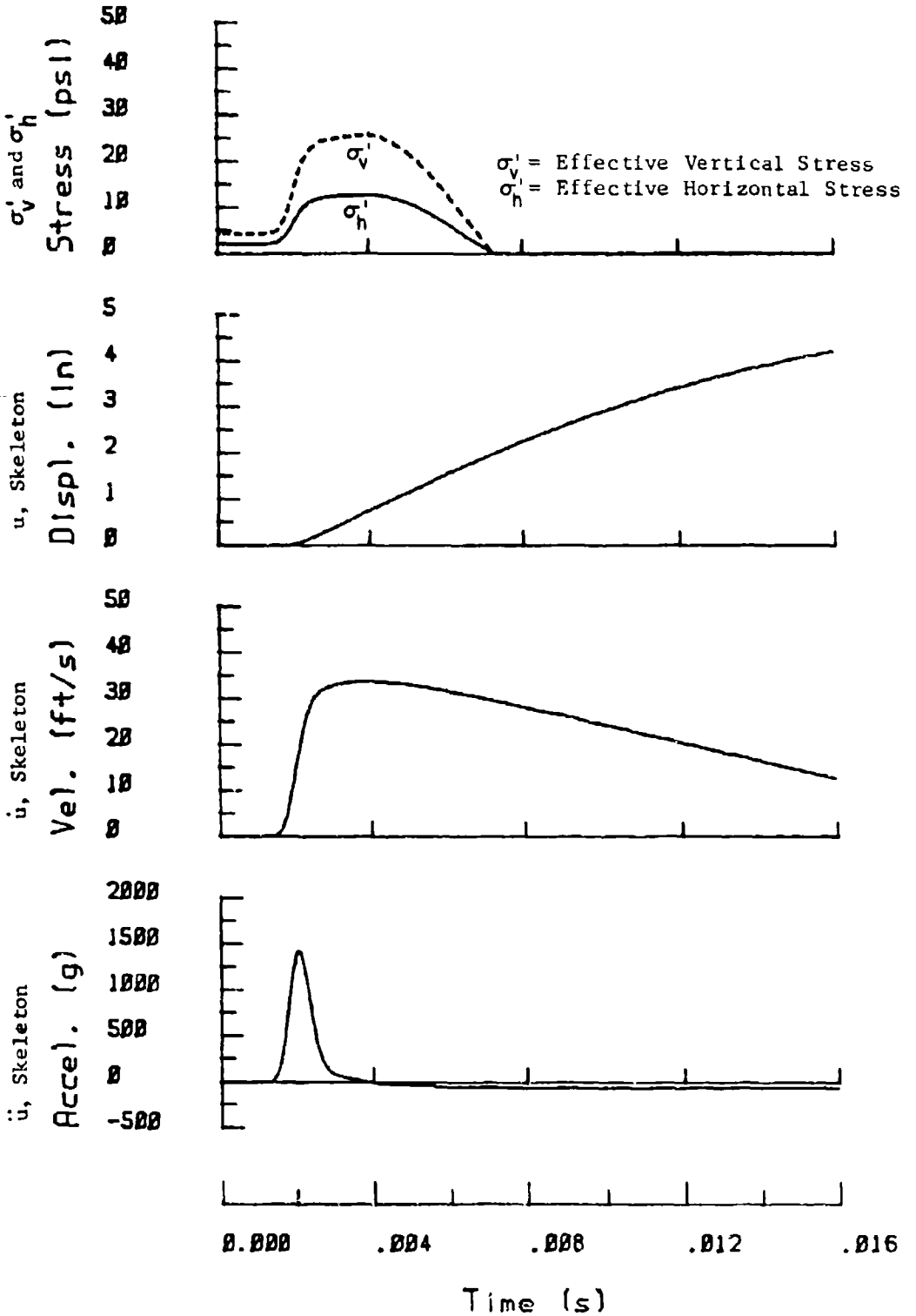

Figure 4.11. Effective stress and skeleton motion time histories at 10 ft depth, 5 ksi triangular loading

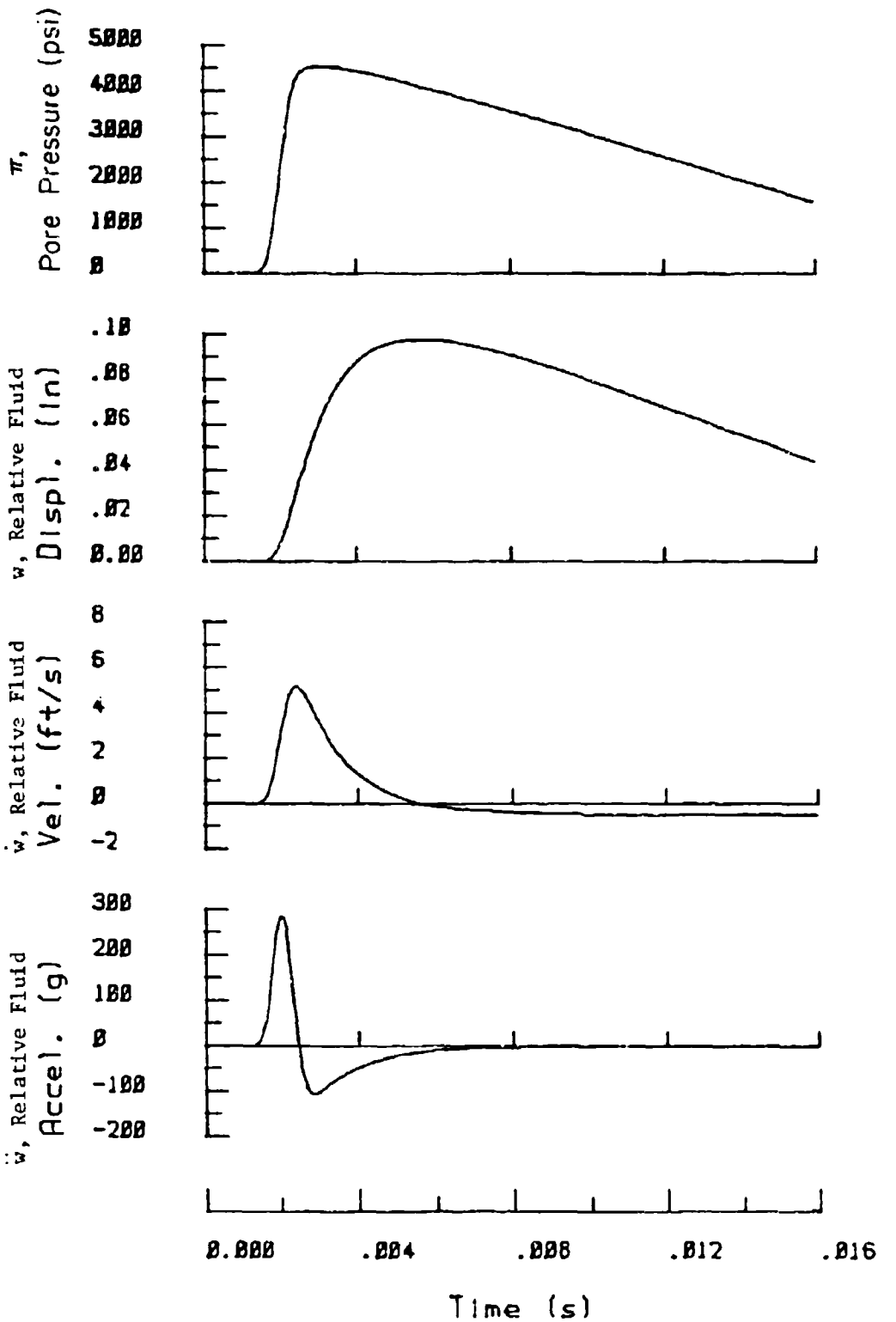

Figure 4.12. Pore pressure and apparent relative fluid motion time histories at 10 ft depth, 5 ksi triangular loading

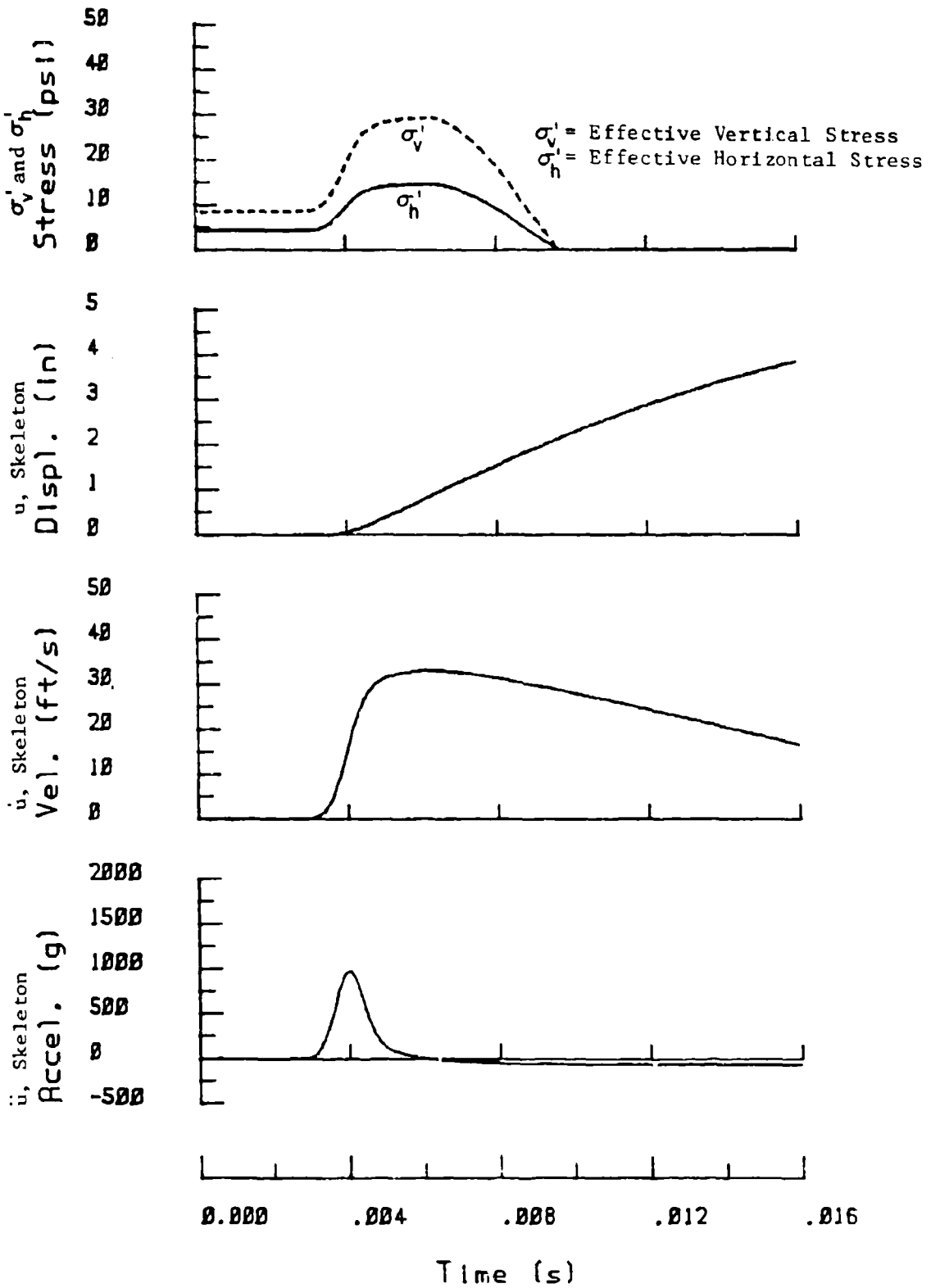

Figure 4.13. Effective stress and skeleton motion time histories at 20 ft depth, 5 ksi triangular loading

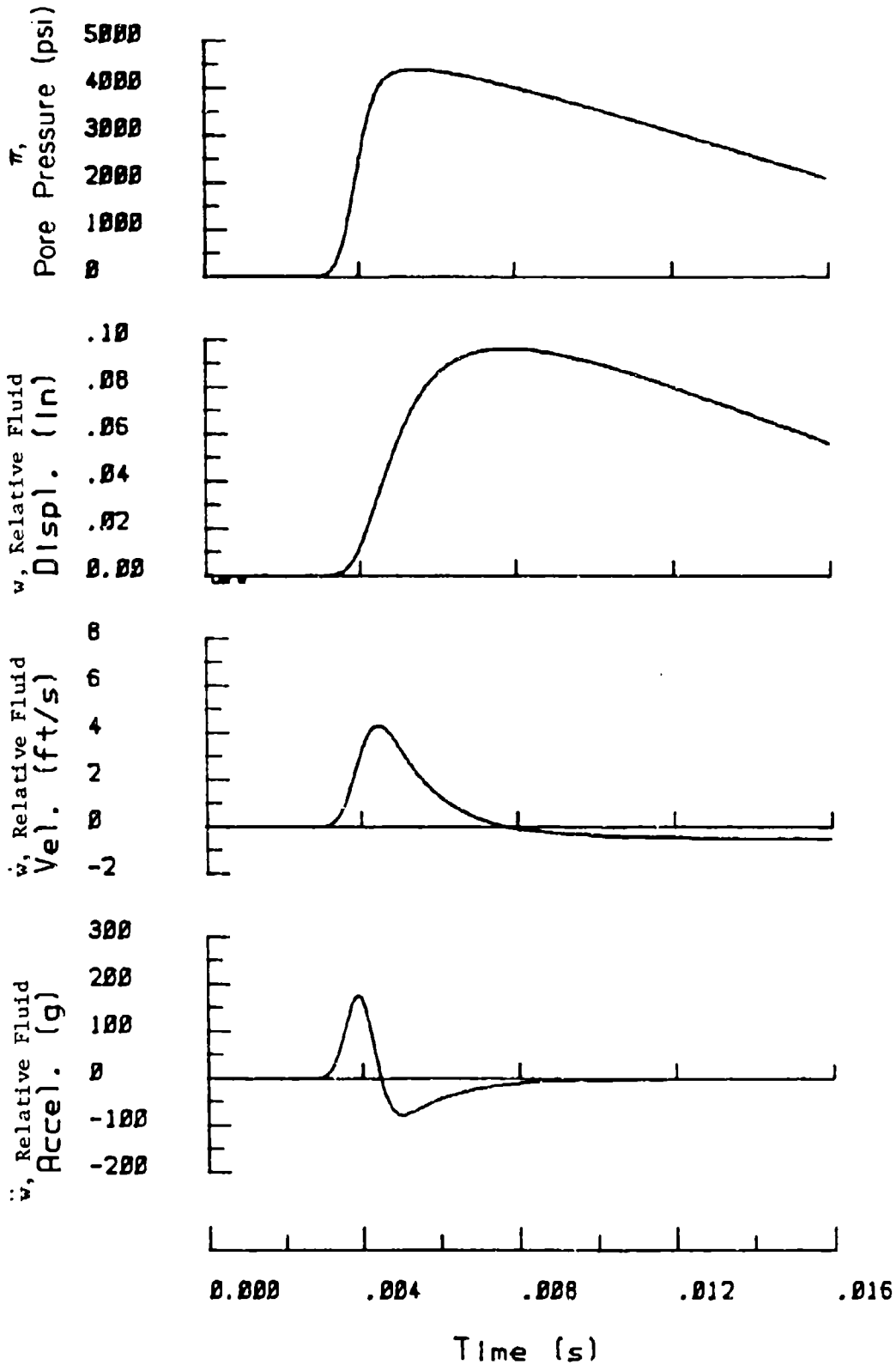

F. e 4.14. Pore pressure and apparent relative fluid motion time histories at 20 ft depth, 5 ksi triangular loading

SECTION 5

SUMMARY AND CONCLUSIONS

The dynamic response of saturated porous media is examined under uniaxial loadings. The material models used in this study become increasingly more sophisticated culminating with an actual saturated sand from Enewetak Atoll. In Section 2, the theoretical background and numerical code, TPDAP, used in this study are described. The governing differential equations of motion for the bulk soil-water mixture and the pore fluid are derived. Biot's fundamental analytic work describing the behavior of saturated porous media is reviewed and summarized. His differential equation for relative fluid motion is generalized by inclusion of the mass increment factor r of Equation 2-60 which accounts for additional friction force resulting from relative acceleration between the pore water and soil skeleton. Biot derived values of r for two simple assumed pore geometries but actual values of r for real soils have not been determined. Values of r for soils should be obtained through a combination of further analytical studies and laboratory investigations. The latter portion of Section 2 presents the finite element formulations used in the TPDAP two phase dynamic analysis program.

Section 3 presents the results of dynamic uniaxial loadings of saturated porous media having a linear elastic skeleton. An analysis of these results produced the following conclusions:

- Use of lumped mass discretization techniques are not suitable for two phase dynamic analysis. Instead, consistent mass techniques are recommended;

- Surface drainage conditions and/or partitioning of the applied load between the pore fluid and soil skeleton only influence the dynamic response in the immediate vicinity of the loaded boundary. Below this zone, the dynamic response is essentially independent of the assumed loading distribution and boundary drainage conditions. To avoid undesirable numerical oscillations caused by large stress gradients, use of an impermeable loading boundary is generally recommended;

- Relative motion between the pore fluid and soil skeleton near the wavefront creates fluid frictional dissipation which tends to smear the wavefront and attenuate the peak stress. These effects are a function of permeability and pore geometry as represented by the mass increment factor, r. As permeability decreases, the dynamic response approaches that obtained using an equivalent one phase analysis. As r increases the relative motions decrease and the dynamic response approaches that of an equivalent one phase loading. Values of r of 1/3 and 1/5, derived for the simplified circular and flat pore geometries, had a negligible influence on the overall dynamic response in these calculations. Larger values of r which may be representative of real soils could have a significant influence on overall response;

- Fluid damping results in more rapid stress attenuation under loadings with more rapid pressure decays;

- Artificial numerical γ damping eliminated high frequency oscillations, but smeared the wavefront at the toe. Minimal artificial damping would have been required in these elastic calculations.

In Section 4, dynamic uniaxial loadings were applied to saturated porous media having a bilinear hysteretic skeleton and the skeleton properties of Enewetak sand. Principal conclusions and observations include:

- Liquefaction occurred in the calculations using both the bilinear and Enewetak hysteretic soil skeletons during the unloading portion of the dynamic response. Liquefaction resulted from non-recoverable strains induced in the skeleton during loading.

- The TPDAP two phase code provides a powerful tool for studying wave propagation in two phase materials. It permits detailed examination of dynamic material response including pore pressure, effective stresses, skeleton motions and relative fluid motions at specified points in time and space. Based on the relative fluid motions, pore water migration and flow rate can be computed.

- Relationships between pore pressure, effective stress, skeleton motion and relative motion between the pore fluid and skeleton were examined in the calculations of the Enewetak sand. During loading, motion of the pore fluid relative to the skeleton is in the direction of

the wave propagation. During the unloading, the relative velocity rapidly decreases and has reversed by the time of liquefaction so that relative motion is opposite to the direction of propagation.

- In situ gravitational stresses can result in an increase in dynamic effective stress during loading with increasing depth and time. The occurrence of such an increase is dependent on the stress strain properties of the soil skeleton and the attenuation characteristics of the soil.

REFERENCES

Archer, J.S., "Consistent Mass Matrix for Distributed Mass Systems," Journal of the Structural Division, ASCE, Vol. 89, No. ST4, pp. 161-178, 1963.

Biot, M.A., "Theory of Propagation of Elastic Waves in Fluid Saturated Porous Solid. I, II," Journal of Acoustical Society of America, Vol. 28, pp 168-191, 1956.

Biot, M.A., "Mechanics of Deformation and Acoustic Propagation in Porous Media," Journal of Applied Physics, Vol. 33, pp 1482-1498, 1962A.

Biot, M.A., "Generalized Thoery of Acoustic Propagation in Porous Dissipative Media," Journal of Acoustical Society of America, Vol. 34, pp 1254-1264, 1962B.

Blouin, S.E., and K.J. Kim, "Undrained Compressibility of Saturated Soil," Draft report to Defense Nuclear Agency, Washington D.C., 13 February, 1984.

Blouin, S.E., Martin, R.J., and K.A. McIntosh, "Laboratory Investigation of the Mechanical Properties of Enewetak Sand," Draft report to AFOSR, June 1984.

Blouin, S.E., and J.D. Shinn, "Explosion Induced Liquefaction," report to Air Force Office of Scientific Research, Washington D.C., 1983.

Bowles, J.E., Physical and Geotechnical Properties of Soils, McGraw-Hill, 1979.

Ghaboussi, J., and E. L. Wilson, "Variational Formulation of Dynamics of Fluid-Saturated Porous Elastic Solids," Journal of the Engineering Mechanics Division, ASCE, Vol. 98, pp 947-963, 1972.

Kim, K.J., "Finite Element Analysis of Nonlinear Consolidation," Ph.D. thesis, University of Illinois, Urbana-Champaign, 1982.

Lysmer, J., and R.L. Kuhlemeyer, "Finite Dynamic Model for Infinite Media," Journal of the Engineering Mechanics Division, ASCE, Vol. 95, No. EM4, pp 859-877, August, 1969.

Mengi, Y., and H.D. McNiven, "Fluid-filled Porous Media to a Transient Input," Journal of Acoustical Society of America, Vol. 61, pp 84-94. 1977.

Richart, F.E., Hall J.R., and R.D. Woods, "Vibrations of Soils and Foundations," Prentice-Hall, Inc., 1970.

Rischbieter, F., et al., "Studies of Soil Liquefaction by Shock Wave Loading," Fifth Intl. Symposium on Military Applications of Blast Simulation, Vol. III, Royal Swedish Fortifications Admin., Stockholm, Sweden, May, 1977.

Scheidegger, A.E., "The Physics of Flow Through Porous Media," Macmillan, New York, 1957.